

Developing High-Performance Lithium Metal Anode in Liquid Electrolytes: Challenges and Progress

Sa Li,* Mengwen Jiang, Yong Xie, Hui Xu, Junyao Jia, and Ju Li*

Lithium metal anodes are potentially key for next-generation energy-dense batteries because of the extremely high capacity and the ultralow redox potential. However, notorious safety concerns of Li metal in liquid electrolytes have significantly retarded its commercialization: on one hand, lithium metal morphological instabilities (LMI) can cause cell shorting and even explosion; on the other hand, breaking of the grown Li arms induces the so-called “dead Li”; furthermore, the continuous consumption of the liquid electrolyte and cycleable lithium also shortens cell life. The research community has been seeking new strategies to protect Li metal anodes and significant progress has been made in the last decade. Here, an overview of the fundamental understandings of solid electrolyte interphase (SEI) formation, conceptual models, and advanced real-time characterizations of LMI are presented. Instructed by the conceptual models, strategies including increasing the donatable fluorine concentration (DFC) in liquid to enrich LiF component in SEI, increasing salt concentration (ionic strength) and sacrificial electrolyte additives, building artificial SEI to boost self-healing of natural SEI, and 3D electrode frameworks to reduce current density and delay Sand's extinction are summarized. Practical challenges in competing with graphite and silicon anodes are outlined.

demand. Therefore it is commonly believed that exploring advanced battery chemistries beyond LIB is a necessity.^[4] In such context, intensive researches on lithium metal batteries (LMBs), including lithium–sulfur,^[5] lithium–air,^[5] lithium metal versus intercalation-type cathodes, etc., are enthusiastically pursued. Compared to state-of-the-art Li-ion cells which deliver an energy density of $\approx 250 \text{ Wh kg}^{-1}$,^[6] cells of Li versus intercalation-type transition-metal oxide (TMO) cathodes such as LiCoO_2 (LCO), $\text{LiNi}_x\text{Co}_y\text{Mn}_{1-x-y}\text{O}_2$ (NCM), LNMO spinel ($\text{LiNi}_{0.5}\text{Mn}_{1.5}\text{O}_4$), and Li-rich NCM ($u\text{Li}_2\text{MnO}_3 \cdot (1-u)\text{NCM}$) could reach a specific energy of $\approx 440 \text{ Wh kg}^{-1}$, and this value could be further boosted, say in Li–S system, to $\approx 650 \text{ Wh kg}^{-1}$, as estimated in Table 1.

In the past few years, there has been significant progress in rechargeable LMBs. For instance, small scale, commercial lithium–sulfur cells were tested by Airbus Defense and Space, which launched their

1. Introduction


Ever-growing market demand for energy storage has supported significant research interests in high-capacity lithium ion batteries (LIB) for portable electronic devices, electric vehicles and even grid-scale storage.^[1–3] However, the existing Li-ion cells are getting closer to their inherent capability limits, unable to meet the relentlessly increasing high-energy-density

prototype unmanned aircraft for an 11 d flight successfully that utilized solar energy during the day and Li–S battery (supplied by Sion Powers with an energy density of 350 Wh kg^{-1}) at night. However, this progress is yet incomplete and the industrial deployment of LMBs has been impeded by the critical problems of battery safety and poor cycling life as well as rate capability, all of which stem from two issues of the Li anodes in liquid electrolytes, namely, solid electrolyte interphase (SEI) formation and lithium morphological instability (LMI). Because liquid electrolytes are typically electrochemically unstable at the potential of Li metal plating, a SEI layer will spontaneously form the moment an electron-conductive surface of the anode is exposed to liquid electrolytes, whenever the anode potential drops below $\approx 1 \text{ V}$ versus Li metal, composed of the insoluble products of the half-cell reaction of solvents and salts. The SEI is essentially a naturally grown solid electrolyte, $1\text{--}10^2 \text{ nm}$ thick, covering the electrode (which, by definition, is both electron-conductive and Li^+ -conductive). The SEI, however, has a transference number strongly favoring Li^+ conduction only (nearly an electron insulator, and also insulating to solvent molecules), and thus in order for the solvated Li^+ in the liquid electrolyte to be reduced, it must shed its solvation shell in the liquid, zip through the SEI by solid-state Li^+ conduction, to be able to meet an electron beneath the SEI. Because the lithium ion conductivity of the as-formed SEI is heterogeneous, inhomogeneous nucleation of lithium metal clusters and subsequent

Dr. S. Li, M. Jiang, Y. Xie, H. Xu, J. Jia
School of Materials Science and Engineering
Tongji University
Shanghai 201804, China
E-mail: lisa@tongji.edu.cn

Dr. S. Li, M. Jiang, Y. Xie, H. Xu
Institute of New Energy for Vehicles
Tongji University
Shanghai 201804, China

Prof. J. Li
Department of Nuclear Science and Engineering and Department
of Materials Science and Engineering
Massachusetts Institute of Technology
Cambridge, MA 02139, USA
E-mail: liju@mit.edu

 The ORCID identification number(s) for the author(s) of this article can be found under <https://doi.org/10.1002/adma.201706375>.

DOI: 10.1002/adma.201706375

Table 1. Li–S cell parameters.

Cathode	1st discharge capacity at 0.1 C [mAh g ⁻¹ based on S]	1000
	Mass loading [mg cm ⁻²]	10
	S content	80%
	Cathode weight including S, conductive agents and binder [mg]	12.5
	Al foil thickness [μm]	12
	Al foil weight ^{a)} [mg cm ⁻²]	3.24
Separator	Weight [mg cm ⁻²]	1
Electrolyte	Electrolyte weight ratio versus S	1.25
	Electrolyte weight [mg cm ⁻²]	12.5
Lithium anode	Li metal thickness [μm]	75
	Li excess amount	50%
	Li metal weight [mg cm ⁻²]	4
Cell	Voltage [V]	2.1
	Energy density ^{b)} [Wh kg ⁻¹]	664

^{a)}Half mass of Al foil is used when calculating the total mass because S is coated on both sides; ^{b)}The energy density is estimated based on a large enough capacity of Li–S batteries, for example, 30 Ah, where the weight of the aluminum–plastic package and lugs could be ignored.

growth might occur, leading to protruding embryos on the electrolyte/electrode interface, even at low current densities long before so-called Sand's time is reached.^[7,8] Furthermore, because neutral Li atom is always deposited beneath the SEI, a compressive stress tends to be generated inside the newly deposited Li metal due to this solid constraint, and a tensile stress tends to be generated in the solid SEI film, as illustrated in **Figure 1a**. If the naturally formed SEI (nSEI) is fragile and brittle, which it typically seems to be,^[9] it will respond to the tensile stress by breaking. This SEI fracture (instead of compliant stretching) is a fundamental issue and the root cause of many problems later on. With SEI fracture, naked lithium metal is exposed to the liquid electrolyte ("flooding"). Whenever there is flooding, new nSEI will form again, isolating the conductive surface from directly touching the liquid and re-achieving "hermiticity," so there is "self-healing."^[10] But a self-healing action due to new nSEI formation will consume electrolyte solvent, salt and cycleable lithium, reflected as a lower Coulombic efficiency (CE) or higher Coulombic inefficiency (CI≡1–CE),^[11] and eventually leads to cell dry out or exhaustion of cycleable lithium.

According to the classical theories of the long-range diffusional instability of dendritic growth, protrusions with high curvature have a considerably stronger electric field at their tips and are also closer to the lithium source, which thus tend to attract more Li-ions, resulting in faster growth of the protrusions and finally evolving into dendrites. The open pores in commercial polymeric separators (typically with opening of tens of nm and length of 10¹ μm) are not able to stop such Li metal dendrites, which can simply plate through them; there are evidences, however, that with even smaller pores, the dendrite might have a harder time penetrating through.^[15,16] These classic models of dendritic instabilities (also shown in **Figure 1b**) based on long-range transport cannot yet satisfactorily described the effects of



Sa Li received her Ph.D. degree in Materials Science and Engineering from Tsinghua University in 2015. Afterward, she joined the School of Materials Science and Engineering at Tongji University as an assistant professor until now. Her current research interest is mainly on designing advanced anode materials for lithium-ion batteries and Li–S batteries.



Ju Li is BEA Professor of Nuclear Science and Engineering and Professor of Materials Science and Engineering at MIT. His group (<http://Li.mit.edu>) performs computational and experimental research on mechanical properties of materials, and energy storage and conversion.

Ju was elected Fellow of the American Physical Society in 2014 and Fellow of the Materials Research Society in 2017.

local heterogeneities and stresses occurring at tens of nanometer scale, such as the SEI-induced stress effect above. The word "dendrite" was originally applied to snowflakes (vapor → solid) and metal casting (liquid → solid) to describe tip-grown morphological instabilities (mode III) driven by long-range mass or heat transport (Mullins–Sekerka instability^[17]). However, because of the stress developed due to the SEI, in electrodeposition of Li metal, it quite often presents "root growth" (mode II) or a combination of root and tip growths (mode I)^[9] instead. Thus, one should be careful when using the word "dendrite." We recommend using the word "whisker" (mode II) for stress-driven root growth, and "dendrite" only for tip-growth after Sand's time is reached (mode III).^[12] If it is not clear whether it was tip-grown or root-grown, a lithium metal "arm" is preferred in this review.

The self-enhancing LMIs cause systemic problems. First, there is a high possibility of cell short circuit if a lithium arm penetrates the separator and reaches the cathode side, resulting in local thermal runaway, sometimes even electrolytes combustion and cells explosion; secondly, as the huge volume change during each plating/stripping cycle for lithium metal anode (LMA) would generate internal stress, some lithium arms could detach from the electrode, and subsequently lose electron accessibility, converting the active lithium to the dead lithium metal. Moreover, the porous or composite nature of LMA would significantly lower its volumetric energy density. Here is a back-of-the-envelope calculation: the theoretical volumetric capacity of fully dense lithium metal is 2062 mAh cm⁻³ (3861 mAh g⁻¹ × 0.534 g cm⁻³),

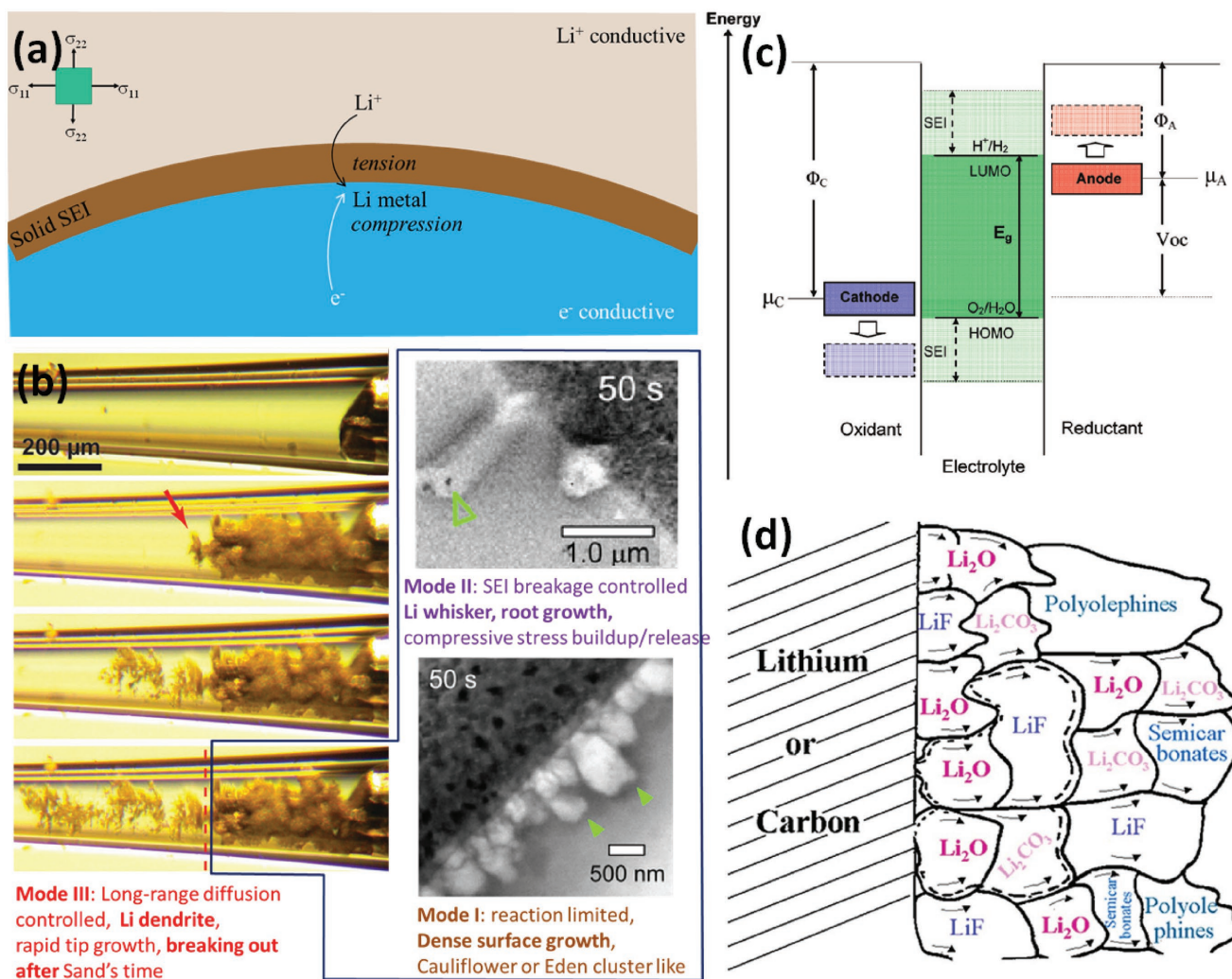


Figure 1. a) Illustration of tensile stress generated in the solid SEI film during lithium electrodeposition. b) Three modes of lithium formation and growth: dense surface growth (mode I), whiskers (mode II), and dendrite (mode III). b) Reproduced with permission.^[12] Copyright 2016, Royal Society of Chemistry, in which the image related to Mode III is additionally reproduced with permission.^[9] Copyright 2017, Elsevier. c) Schematic energy diagram of liquid electrolytes. Φ_A and Φ_C represent work functions of the anode and cathode, respectively. Reproduced with permission.^[13] Copyright 2009, American Chemical Society. d) Schematic illustration of microstructured SEI films. Reproduced with permission.^[14] Copyright 1997, The Electrochemical Society.

which gives fully dense Li an initial $3.5 \times$ advantage versus graphite ($372 \text{ mAh g}^{-1} \times 1.6 \text{ g cm}^{-3} = 600 \text{ mAh cm}^{-3}$). However, with continuing lithium dendrites growth, once the nonlithium volume fraction ($\phi \equiv 1 - \rho/\rho_{\text{ideal}}$) exceeds 70%, LMA will not be commercially competitive against graphite. Besides, these pore- and SEI-rich Li deposits would also increase impedance to Li-ions/electrons and render a growing overpotential, a manifestation of huge internal resistance and a large polarization. (We have seen gas bubbles generated due to large overpotential,^[15] which will further exacerbate porosity and impedance.) Although an externally applied compressive stress when testing Li metal batteries can be effective to some extent, it seems unrealistic to apply too much load with liquid electrolyte, especially in the Li-S system where the sulfur cathode is sensitive to stress.

In this review, we first provide a fundamental understanding of SEI formation (Section 2.1) and balance-of-plant principles in constructing LMB (Section 2.2) where the terminology

of Coulombic inefficiency and prelithiation ("0.5 \times excess," "2 \times excess," etc.) is introduced. The benefits of LiF and high donatable fluorine concentration (DFC) are explained for constructing parsimonious Li excess and parsimonious electrolyte, high-performance, full cells. This followed by a qualitative overview in Section 3.1 of the long-range transport induction of LMI (Sand's extinction as the ionic strength goes to zero) where we distinguish between tip-grown true dendrite (mode III) from root-grown whisker (mode II), as well as stress developments and inelastic creep/fracture in the SEI and the Li metal, in Section 3.2. The take-home message is that low anion transference number t_- (delaying Sand's singularity) and high ionic strength/salt concentration (reducing flammability and changing highest occupied molecular orbital (HOMO)/lowest unoccupied molecular orbital (LUMO) levels) are desirable. Simultaneously, SEI fracture should be avoided by high-toughness nSEI, artificial SEI (aSEI) reinforcements, or soft stretchy

sticky solid (4S) electrolyte, without increasing the cell impedance too greatly. Both discrete-agent-based and continuum numerical models of LMI were reviewed (Sections 3.3 and 3.4). A considerable number of experimental methods that were able to suppress LMI and enhance Coulombic efficiency have been shown (Section 4). Finally, recent progresses of the in situ characterization methods of the lithium deposition in LMBs, including in situ optical microscopy, electron microscopy observations as well as some other newly developed techniques, are highlighted (Section 5). In this review, particular attention is paid to the conceptual models (Sections 2, 3.1, and 3.2) as a reference frame to explore the effects of current density, electrolytes components, surface state of anodes on LMI, which also guide the lithium metal protection (Section 4) experimentally.

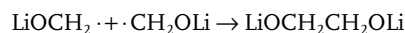
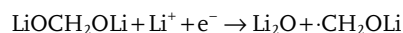
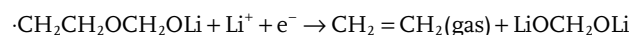
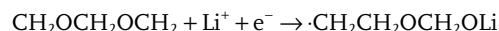
2. Challenges of Lithium Metal Anodes in Liquid Electrolytes

Several formidable challenges, both scientific and technological, need to be addressed before the industrial deployment of LMBs.

2.1. SEI Formation

Body-centered cubic (BCC) lithium metal ($a_0 = 3.51\text{\AA}$) is a well-known anode candidate with a very negative equilibrium potential (-3.04 V vs the standard hydrogen electrode), which grants LMBs a high voltage and also a high theoretical energy density (theoretical capacity of lithium metal anode is 3861 mAh g^{-1} , or 2062 mAh cm^{-3} when fully dense). Even if the cathode functions impeccably (which it never does), the lithium metal anodes with the ultralow potential and high reactivity could result in chemical and morphological instabilities at the interface with electrolytes in rechargeable batteries. The thin film formed by the reaction of electrolytes and Li was first discovered by Dey in 1970^[18] and defined as “SEI” by Peled in 1979.^[19] Goodenough et al. explained the relationship between the SEI formation on electrodes and the LUMO/HOMO of electrolytes (Figure 1c).^[13] When the electron's chemical potentials (cathode: μ_C or anode: μ_A) go outside the electrochemical stability window of electrolyte, an electron escape (oxidation reaction) or electron injection (reduction reaction) event will happen to the solvent molecule or ions in the liquid electrolyte as half-cell reactions until a thick enough passivation layer (SEI) is formed on the electrode. In this regard, electrode materials should be chosen to well match the electrochemical stability window of the electrolyte to avoid serious interphase reactions. Unfortunately, the $\mu_A \equiv -eU_{\text{Anode}} = \varepsilon_F$ (Anode) of lithium metal is located well above the LUMO of practically used organic electrolyte solvent molecules (such as ethylene carbonate (EC), propylene carbonate (PC), diethyl carbonate (DEC), dimethyl carbonate (DMC), etc.) and anions (such as PF_6^- , TFSI^- , FSI^- etc.), at least when the salt concentration is low like 1 M .^[13,20,21] When bare Li is exposed to electrolyte, a serious reduction reaction will be initiated between free electron in the lithium and electrolyte solvents and salts in time of milliseconds or even less.^[22]

Under a constant potential $U_{\text{Anode}} < 1.2\text{ V}$, the growth of SEI would be stopped when the kinetics of electron transport (from inside to outside) and solvents transport (from outside to inside) become too sluggish.^[22,23] So the thickness of SEI is determined by the electron tunneling/diffusive hopping as well as solvent diffusion penetration depth.^[24] A typical thickness of SEI ranges from a few to several hundreds of nanometers, but this is hard to measure very precisely due to its air instability and considerable variation with the electrolyte components and environment (such as temperature, pressure, current density, voltage and so on).^[22,25] The chemical constituents of the SEI formed on lithium metal anodes are largely determined by the reductive activation of solvents, salts, additives or impurities in electrolytes. When lithium metal anodes came into direct contact with liquid electrolyte (“flooding”), reductive decompositions would be initiated immediately resulting in a mixture of insoluble multiphase products deposited on the surface of anodes. Taking 1,3-dioxolane (DOL, $\text{CH}_2\text{OCH}_2\text{OCH}_2$) as a liquid solvent, for example, the following sequence of reactions might occur



As a matter of fact, the constituents of SEI can be far more complicated, considering the electrolyte salts, additives and even trace water could also be involved in the half-cell reactions, and ultimately, a combination of organic and inorganic species would be formed on the lithium metal anodes, as proposed by Peled in the mosaic model (Figure 1d),^[19] where the inhomogeneity of SEI not only on parallel direction but also on the vertical direction was indicated. Recently, advanced analytical techniques, such as scanning electron microscopy (SEM), X-ray photoelectron spectroscopy, Fourier transform infrared spectroscopy, nuclear magnetic resonance (NMR) and so on, have been applied to component analysis of SEI films. Up to now, although it is still undoubtedly challenging to precisely identify their complete chemical composition, it has been widely accepted that SEI films have a dual-layer structure in the thickness direction,^[20,22,26] namely, an outer organic layer comprising species with a high oxidation state, such as ROCO_2Li and ROLi (R is an organic group related to the solvent), and an inner layer that tightly clings to the metallic Li surface mainly containing species of low oxidation states, for example, Li_2O , Li_3N , LiF , and Li_2CO_3 .

Based on the previous discussions, ideally speaking, a perfect SEI should have the following characteristics:

Electronic: It should be highly electron-insulating, so even a very thin nSEI can stop electron tunneling, thereby shutting off the growth in thickness naturally—in other words a very thin nSEI can finish the passivation, and do not require too much materials from liquid to build, or repair after a flooding event.

Generally speaking, materials with wide bandgap have the fastest electron tunneling decay, thus LiF, with extremely large bandgap of 13.6 eV, and electrochemical stability against both Li metal and high-voltage cathodes,^[27] should be a good candidate as nSEI component.^[28]

Mechanical: An ideal SEI should be mechanically tough in-plane (“stretchy”) to avoid bursting. Like good clothing material, it should be difficult to tear. But if such layer is very thin, it may not want to stick too much to the substrate either to minimize the generation of stress.^[10] If it is thick but soft and stretchy, it may afford to be sticky—the so called 4S electrolyte.^[15,29] However, nSEI typically cannot achieve such mechanical performance, and thus reinforcements by aSEI^[10] might be helpful. aSEI (like “sheet material”) should have good adhesion with nSEI (like “mud”) to form a “mud hut” to achieve ad hoc hermiticity.^[10] Also, even though LiF is a ceramic, it is actually plastically deformable at room temperature in water-free environment, and thus it might be able to deform under tension in a ductile fashion rather than brittle fracture.^[28]

Ionic: The nSEI (and aSEI) need to allow naked Li⁺ ion to diffuse through, while forbidding transport of electron and solvent molecules across it. The Li⁺ ion conductivity could be a problem for 4S electrolyte^[15,29] because they tend to thicker than nSEI.

Because nSEI is generated by decomposition of the liquid electrolyte, by tuning the chemistry of the liquid electrolyte, the properties of nSEI can be tuned. Liquid electrolyte with high DFC can give nSEI with higher LiF, and indeed it was shown that CI $\equiv 1 - CE^{[11]}$ of lithium metal cycling decays roughly exponentially with increasing DFC of the liquid electrolyte,^[28] which provides a key guidance on selecting liquid electrolyte for the longevity of the LMB. Here, donatable fluorine is counted not by the total number of F atoms in the liquid electrolyte, but only those F in salt/solvent molecules whose half-cell reduction is postulated to generate LiF. As shown by first-principles simulations of the reduction of Li salt and solvent,^[30,31] “the number of LiF generated per LiClO₄, lithium bis(trifluoromethanesulfonyl) imide (LiTFSI), lithium bis(fluorosulfonyl)imide (LiFSI), and fluoro ethylene carbonate (FEC) molecule is 0, 1, 2, and 1, respectively. DFC is thus defined straightforwardly as the molar sum of donatable F of salt and solvent molecules in 1 liter of mixed electrolyte solution.”^[28]

Take 1 M LiFSI-FEC, for example (1 mol of LiFSI salt mixed in originally 1 L of pure FEC solvent). LiFSI has molecular weight 187.07, FEC has molecular weight 106.05. So 1 L of pure FEC (density of FEC: 1.41 g cm⁻³) weighs 1410 g, and 1 mol of LiFSI weighs 187.07 g. The mass ratio of salt and solvent in the electrolyte is then 11.7% and 88.3%, respectively. The mixed solution has a density of 1.51 g cm⁻³, so 1 L of mixed solution weighs 1510 g, and contains 1510 × 88.3%/106.05 = 12.57 mol of FEC, and 1510 × 11.7%/187.07 = 0.9455 mol of LiFSI. Thus the total number of donatable fluorine in 1 L of mixed solution is 0.9455 × 2 + 12.57 = 14.4617 mol, and the DFC is therefore 14.4617, with the majority of the contribution from the FEC solvent. Yet, with increasing salt fraction to 7 M LiFSI-FEC, the contribution from salt and solvent would become nearly 50%:50%.

The computed DFCs for some electrolytes are listed in **Table 2**. As shown in ref. [28], ⟨CI⟩ decays nearly exponentially with DFC across many electrolytes, suggesting that LiF indeed serves as an effective nSEI component.

Table 2. DFC of different F donated electrolytes (taken from ref. [28]). Here 1 M stands for 1 mole of salt added to 1 liter of (originally) pure solvent.

Electrolyte	Salt [mol]	Solvent [L]	Density [g cm ⁻³]	DFC
1 M LiClO ₄ -PC	1	1	1.24	0
1 M LiTFSI-PC	1	1	1.27	0.851
1 M LiFSI-PC	1	1	1.26	1.810
1 M LiFSI-FEC	1	1	1.51	14.46
2 M LiFSI-FEC	2	1	1.56	15.12
3 M LiFSI-FEC	3	1	1.58	15.47
4 M LiFSI-FEC	4	1	1.60	15.79
5 M LiFSI-FEC	5	1	1.61	15.99
6 M LiFSI-FEC	6	1	1.66	16.58
7 M LiFSI-FEC	7	1	1.68	16.86

2.2. Design Principles of Rechargeable LMBs

A rechargeable battery has the following system characteristics: voltage $V \equiv U_{\text{cathode}} - U_{\text{anode}}$, where U_{cathode} , U_{anode} are the absolute electrode potentials with respect to some reference, typically bulk Li metal; capacity Q (number of electrons flown through the outer circuit); mass $M \equiv M_{\text{cathode}} + M_{\text{anode}} + M_{\text{separator}} + M_{\text{electrolyte}} + M_{\text{packaging}}$, where M_{cathode} or M_{anode} includes masses of the active material, binder, current collector and conductive agents maintaining electron percolation, and nSEI/aSEI; and volume $\Omega \equiv \Omega_{\text{cathode}} + \Omega_{\text{anode}} + \Omega_{\text{separator}} + \Omega_{\text{packaging}}$. A lot of these variables depend on Q (state of charge, or state of discharge): $U_{\text{cathode}}(Q)$, $M_{\text{cathode}}(Q)$, $M_{\text{anode}}(Q)$, $\Omega_{\text{cathode}}(Q)$, $\Omega_{\text{anode}}(Q)$, etc. Full-cell performance is often evaluated by the discharge gravimetric energy density $\langle V \rangle Q_{\text{max}}(\text{discharge})/M$, where $\langle V \rangle$ is the average voltage between $Q = 0 \dots Q_{\text{max}}(\text{discharge})$; volumetric energy density $\langle V \rangle Q_{\text{max}}/\Omega$; gravimetric and volumetric power densities, i.e., rate capabilities, in particular the charging rate is often the bottleneck; cycle life, self-discharge rate and shelf life; energy efficiency, that is, $\eta \equiv \langle V \rangle Q_{\text{max}}(\text{discharge})/\langle V \rangle Q_{\text{max}}(\text{charge})$; low- and high-temperature capabilities; and finally, safety characteristics in normal and abuse situations. The liquid electrolyte is the working fluid of the battery and controls all the key aspects above. For example in Li-S batteries, $M_{\text{electrolyte}}$ is often the dominant component in M and dwarfs M_{cathode} , M_{anode} ,^[32] thus how much electrolyte used in the cell is the most important decision for gravimetric energy/power densities and cycle life. In terms of safety, the high vapor pressure of organic electrolytes, and the large surface area of Li metal (due to morphological instabilities above^[9]) after cycling, means that once the packaging is compromised, a hot cell may quickly explode. Thus electrolyte additives that suppress liquid electrolyte volatility and flammability are often used. The high- U capability of electrolyte, namely the electrochemical stability window of the electrolyte on the U_{cathode} side, often controls the voltage range of the battery.^[28] The chemical compatibility of electrolyte with sulfur, and solubility of transition-metal Mn, Ni etc. ions in the electrolyte largely determine the choice of cathode materials (Li-S, Li-O, or Li-TMO) that the LMB can adopt for a given electrolyte: thus ether electrolytes which show superior performance for Li-S and Li-O batteries may not be useable for Li-TMO due to the higher U_{cathode}

required. Electrolyte characteristics such as Li^+ conductivity and Li^+ transference number t_+ are obviously important, in particular, a low anion transference number $t_- = 1 - t_+$ is known to suppress Li metal dendrite instabilities, due to delayed onset of Sand's singularity (defined by the complete depletion of anions in the electrolyte approaching electrode–liquid interface).^[33] The viscosity of the liquid electrolyte (which tends to depend on the temperature sensitively), and the wettability of this liquid electrolyte with porous electrodes such as sulfur cathode, are often key for device processing and performance. Finally, cost is a big issue for industrial applications: for example, room-temperature ionic liquids which are organic molten salts without solvent, possessing good characteristics such as high ionic strength (which delays LMI), low vapor pressure and thus flammability, are still about 20× more expensive than common LiPF_6 in carbonates electrolytes. In addition, while we know high-DFC liquid electrolyte brings exponentially longer cycle life,^[28] fluorinated chemicals tend to be more expensive. In this backdrop, finding liquid electrolytes that also work with Li metal with high reversibility is quite a daunting task.^[28]

Because selecting liquid electrolyte is so complicated, it is easy to make the mental mistake of over-emphasizing certain good characteristics while sweeping bad characteristics under the rug. The most robust way to evaluate a certain electrolyte is still to make a full-cell (preferably > 1 Ah, e.g., >500 cm^2 of >2mAh cm^{-2} cathode/separator/anode periods), with lithium metal anode of initially limited excess (see below) paired with a well-known cathode like LiFePO_4 , and test the full-cell cycle life. Like how a team leader should be evaluated, the best electrolyte should be the one that leads to the best team score, rather than the member that strikes the most personal scores. With this in mind, in designing any full-cell LIB, it is essential to keep in mind the “balance of plant” (BOP) principle. This is because in order for Q electrons to flow through the outer circuit, several processes have to happen in synchrony inside the battery. Simplistically, Q Li^+ ions need to leave (or join) the cathode into the electrolyte, the electrolyte needs to transport these ions from cathode side to the anode side, and the same number of ions needs to be deposited into the anode. (We say simplistically, because other soluble species, so-called soluble redox mediators (SRM), may diffuse in the liquid electrolyte and transport and transfer Faradaic charge in a nonblocking manner, like the well-known $\text{Fe}^{2+}/\text{Fe}^{3+}$ couple in aqueous electrochemistry. Indeed, SRMs may be generated afresh every time after a SEI breakage and “flooding” event as soluble products of decomposition reactions, in contrast to the insoluble products which form SEI. SRM and SEI thus may have an interesting causal relationship.) In principle, therefore, the cathode-active and anode-active materials should have matching areal capacities,^[11] and $M_{\text{electrolyte}}$ should be reduced as long as long-range ionic percolation can be maintained, to maximize full-cell energy density. This BOP principle was ignored in so-called “half-cell” tests, where superabundant counter-electrode (and typically superabundant liquid electrolyte) is used against the working electrode, because presumably only the single-electrode material characteristics are considered interesting. However, “half-cell” tests tend to mask certain deficiencies. It is strongly recommended, especially with alkali metal anodes, to perform both “half-cell” test without BOP, and “full-cell” test with BOP

against some well-known cathode material like LiFePO_4 (LFP) or LCO, to contrast the cycling results, which helps to separate different degradation mechanisms.^[34]

Some language and definitions are helpful for BOP of rechargeable LMBs. If one chooses to use TMO cathode such as LiFePO_4 , LiCoO_2 , etc., these materials typically come with its own full complement of cycleable lithium. Thus, an ideal rechargeable LMB could conceptually use just a bare copper collector on the anode, and would be able to cycle forever, as the TM atom changes valence $\text{TM}^{m-1} \leftrightarrow \text{TM}^m$ to accommodate Li^+ in and out of the cathode, and Li metal is plated and stripped as compact dense film on the copper current collector. This is called “Li-free” or “0 × excess” full-cell, which is the ideal construction.^[28] However, because in reality SEI necessarily will build up on the anode (and perhaps also at the cathode) which converts some cycleable lithium to noncycleable lithium, the 0 × excess LMB cannot demonstrate very high performance in practice, because for the every noncycleable lithium atom trapped in SEI, there is a “widowed” Co/Ni/Mn/Fe atom in the cathode with unchanged valence during cycling ever thereafter—these atoms are much heavier, and in the case of Co/Ni, much more expensive than the trapped Li, thus decreasing the gravimetric and cost performances of the full cell. To compensate for this, various means of “prelithiation” should be considered,^[10] which means the system has to bring in extra or excess cycleable lithium in some way. For example, if we use LiFePO_4 cathode with nameplate capacity 3 mAh cm^{-2} , then with “Li-free” or “0 × excess” full-cell we should use just bare copper collector in direct contact with separator, with nothing extra in between. Then after electrolyte injection and a fully charge, suppose there were no SEI, and the deposited Li metal film were fully dense and flat, then 3 mAh cm^{-2} /2062 mAh cm^{-3} = 3 × 4.85 μm ≈ 15 μm of dense Li metal film should be deposited on Cu as $\text{LiFePO}_4 \rightarrow \text{FePO}_4$, and this lithium metal film is supposed to cycle as 15 μm ↔ 0 μm thereafter. But since there is loss in the first cycle (“formation”) and thereafter (“self-healing”), if we use a lithium metal foil 30 μm before electrolyte injection during the full-cell construction, against the 3 mAh cm^{-2} LiFePO_4 , we will call this a “2 × excess” LMB. Clearly, a “2 × excess” LMB should give longer cycle life than the “0 × excess” or “Li-free” construction, at the expense of lower initial energy density. One may also choose a “0.5 × excess” configuration, which is an initially 7.5 μm lithium metal foil against 3 mAh cm^{-2} LiFePO_4 before electrolyte injection. The “0.5 × excess,” “1 × excess,” “1.5 × excess,” etc. is a design freedom that one can choose in constructing the full cell, taking into view the desired cycle life, initial and steady-state Coulombic inefficiencies, etc. that have much to do with the exact liquid electrolyte used.^[28] However, it will generally not make too much sense to use more than “3.5 × excess” in a full cell (e.g., 50 μm lithium metal foil countering 3 mAh cm^{-2} nameplate cathode), because then the full-cell volumetric energy performance will then lag behind using graphite anode, as the graphite thickness countering 3 mAh cm^{-2} nameplate cathode is just about 60 μm ,^[11] with much better Coulombic efficiencies and cycle life. Testing a LMB full cell with parsimonious Li-excess and parsimonious electrolyte is the best way to test the true performance of an electrolyte. Recently, Suo et al. has constructed a high-voltage ($V = 4.7$ V) LMB using $\text{LiNi}_{0.5}\text{Mn}_{1.5}\text{O}_4$ cathode with only 1.4 × excess lithium metal,

and demonstrated stable full charge–discharge at an industrially relevant areal capacity of $\approx 2 \text{ mAh cm}^{-2}$ and 0.36C, over 130 cycles, based on a series of ultraconcentrated full-fluorine electrolytes with extremely high DFC.^[28]

If, on the other hand, pure sulfur or open-air oxygen cathode is used, then the cathode does not come with any cycleable lithium with it, so the “Li-free” construction is not applicable in such scenario. (The so-called solid-oxygen^[35] or lithium sulfide^[36] batteries have a different construct.) In such cases, “0 × excess” is defined as the initial lithium metal foil thickness matching the nameplate capacity of the cathode; “2 × excess” would therefore mean the thickness is 3 × cathode areal capacity/(mAh cm⁻²) × 4.85 μm. For example, suppose from half-cell tests we know a particular sulfur cathode has areal capacity 5 mAh cm⁻², then a “0 × excess” full cell will come with a 1 × 5 × 4.85 μm = 24.2 μm lithium foil before electrolyte injection, by definition; whereas a “2 × excess” full cell will come with a 3 × 5 × 4.85 μm = 72.7 μm lithium foil, before electrolyte injection, by definition. Again, to evaluate the performance of a certain LMA in a certain liquid electrolyte, it is key to evaluate its Coulombic efficiency^[11] (as a sign the efficacy of self-healing^[10]) in half cell, as well as full-cell performance with parsimonious Li-excess such as 0.5 ×, 1 ×, or 2 × excess. It would not make much sense commercially to use more than 3.5 × excess, if volumetric energy density is a concern.

For LMA the Coulombic efficiency, by default, should be defined by the following “clean-slate” measurement procedure: (1) In the “prep” leg, pull all the cycleable lithium out of the anode by raising U_{anode} until a cutoff $U_{\text{anode}}^{\text{upper}}$ is reached, to make sure there is no cycleable lithium left on the copper (there might be dead lithium inside the SEI, but they cannot be pulled out); (2) Deposit some cycleable lithium back to this anode: since Li⁺ flux in the liquid electrolyte cannot be directly measured in typical electrochemical tests and it has to resort to counting electrons outside to infer what happens inside, when $Q_{\text{reduction}}$ electrons was counted flowing through the outer circuit, it’s simplistically assumed $Q_{\text{reduction}}$ Li⁺ ions are indeed sent into the anode in deposition; (3) Strip lithium by reversing current direction again, and pull out all the cycleable lithium out of the anode again by $U_{\text{anode}} \rightarrow U_{\text{anode}}^{\text{upper}}$, and count $Q_{\text{oxidation}}$ electrons flowing through the outer circuit. One then defines CE $\equiv Q_{\text{oxidation}}/Q_{\text{reduction}}$. If still simplistically assuming that $Q_{\text{oxidation}}$ Li⁺ ions are actually pulled out of the anode, then the CE value can be interpreted as the ratio of cycleable lithium that can be pulled out following deposition of certain number of cycleable lithium into a cleaned-out LMA. CI $\equiv 1 - \text{CE}$ may then be interpreted as the fraction of cycleable \rightarrow noncycleable lithium conversion in this round, presumably lost to the SEIs, and $Q_{\text{reduction}}$ CI as the net transfer of Li atoms from the cathode side to the anode side. In the following cycles, step 1 may be omitted if the stripping assumed to have cleaned the slate (cycleable lithium inventory in anode) in the previous cycle completely, like emptying out a bank account.

CI is the most important electrochemical characteristics of the LMA, and is the most critical parameter for the longevity of LMB. There is an industry lore that CI needs to be 0.1%, or CE needs to be 99.9%, in order for a rechargeable battery to cycle 200 times. This is because if 0.1% of the cycleable lithium is really lost forever per cycle, then clearly the LMB full-cell

capacity will decrease exponentially with number of cycles, and $(0.999)^{200} \approx 80\%$. According to this interpretation of CI, one needs 99.99% CE, to sustain thousands of cycles. It is not easy to resolve 99%, let alone 99.99%, on the axis of a linear graph. Therefore it is recommended to plot CI on a logarithmic scale versus the cycle number,^[10] instead of the typical practice in the literature of plotting CE in the linear scale.

In the first few cycles, CI tends to be especially large, as the nSEI are being formed en masse on the current collector and/or artificial host of LMA. For comparison, commercial graphite anode has a first-cycle CE > 92%, and it increases to above 99.5% within 5 cycles. Such performance is rarely found in LMA today. So commercial graphite anode shows a much longer cycle life in BOP full cells. Another important characteristics is the anode expansion strain: currently, cell manufacturers will not accept anode thickness expansion of more than 20%, that is, $\Omega_{\text{anode}}(n)/\Omega_{\text{anode}}(0) < 1.2$, where n the cycle number. LMA clearly also lacks in this regard, as the amount of expansion tends to be huge. Some of competitors to LMA, such as Si-containing anode, start to demonstrate CE > 99.99% and manageably small expansion (albeit after a long formation process).^[10] These are important considerations for LMA if it competes on the marketplace.

However, due to the complication of SRMs,^[11] the quantitative interpretation of CI is more involved actually. Empirically, the so-called Coulombic inefficiency cumulant analysis seems to give overly pessimistic predictions compared to the actual full-cell capacity decay, by few folds.^[11,34] Also, the measured CI_n may even be negative. One does not need to invoke SRMs to explain this. Imagine a lithium metal “flotsam” particle^[9] buried inside SEI debris that has lost electrical contact with the current collector. During the “prep” leg (step 1), this lithium metal particle was not activated because of the loss of electron percolation, so even though we think the slate is cleaned, it is not really. Then, during the deposition (step 2), as new lithium metal is injected into the LMA, there are stress and strain evolutions in the LMA and SEI debris are being pushed around, so electron percolation to this lost particle may be somehow re-established. Then, in the stripping process (step 3), this previously lost particle may contribute to $Q_{\text{oxidation}}$, so it might end up with $Q_{\text{oxidation}} > Q_{\text{reduction}}$, CE > 1 and CI < 0, for this round of measurement at least.

Philosophically, the Coulombic inefficiency is also only one of the several key characteristics. One should not be able to ascertain the full picture within LMB with just {CE_n}.^[11] Measuring the weight gain of the cathode/anode ($\Delta M_{\text{cathode}}$, ΔM_{anode}) and the thickness change ($\Delta \Omega_{\text{cathode}}$, $\Delta \Omega_{\text{anode}}$), for example, are also excellent (and perhaps more robust) indicators of how well the liquid electrolyte is behaving with the electrodes. The main problem is that these measurements, if done in operando, are technically more challenging; but instrumentation issues are getting improved all the time (see Section 5).

3. Conceptual Models and Numerical Simulations

LMI, lithium flotsams, and other noncycleable lithium^[9] impact CI, cycle life, and safety of LMB, while the growth of non-lithium volume fraction ($\phi \equiv 1 - \rho/\rho_{\text{ideal}}$) in the LMA, filled up by SEI (solid) or gas, reduces the energy and power densities of

LMA. These two factors limit the practical competitiveness of LMA against graphite or silicon anodes. Below, we will review some classic models of lithium metal morphological instabilities, keeping in mind that tip-grown dendrite (mode III) is only one mode of LMI.

3.1. Sand's Time Model

Lithium metal deposition can be viewed as a combination of mass transport in the liquid and electron transfer at the interface, which means, lithium ions in the liquid electrolyte would arrive at the electrolyte–electrode interface, shed its solvation shell, diffuse through the SEI and accept an electron to become a neutral lithium metal atom buried beneath the SEI. (Following this, there is also a lithium solid elasticity/plasticity problem, which we deal at the end of this section.) The solvent molecules and anions are supposed to not participate in the reactions once the SEI has been fully established, that is, they may be transported in the liquid, but do not react at steady-state, as both electrodes appear to them as “blocking.”

Through the pioneering work of Sand^[7] and Chazalviel,^[37] the long-range mass transport aspects of this problem have been elucidated, in particular the critical role of anion depletion near the LMA in triggering LMI.^[33] Consider Li^+ cation concentration of $c_+(\mathbf{x})$, and a monovalent anion like PF_6^- whose concentration is $c_-(\mathbf{x})$ [unit 1 m^{-3}]. Inside the electrolyte, the cation and anion fluxes are

$$J_+(\mathbf{x}) = -D_+ \nabla c_+(\mathbf{x}) + e\mathbf{E}(\mathbf{x})(D_+/k_B T)c_+(\mathbf{x}) + c_+(\mathbf{x})\mathbf{v}(\mathbf{x}) \quad (1a)$$

$$J_-(\mathbf{x}) = -D_- \nabla c_-(\mathbf{x}) - e\mathbf{E}(\mathbf{x})(D_-/k_B T)c_-(\mathbf{x}) + c_-(\mathbf{x})\mathbf{v}(\mathbf{x}) \quad (1b)$$

where the first terms are due to chemical potential gradient and D_+ , D_- [unit $\text{m}^2 \text{ s}^{-1}$] are the cation and anion diffusivities, the second terms are due to electrostatic potential gradient $\mathbf{E}(\mathbf{x}) \equiv -\nabla\phi(\mathbf{x})$ inside the liquid, and the third terms are due to convection where $\mathbf{v}(\mathbf{x})$ is the electrolyte convection velocity [unit m s^{-1}] as a whole.^[38] In the above we have ignored the Onsager cross-coupling effect, thus the cation and anion mobilities are $m_+ \equiv D_+/k_B T$, $m_- \equiv D_-/k_B T$, which are exact in the dilute $c_+(\mathbf{x})$, $c_-(\mathbf{x})$ limit. We have also ignored SRMs. The cation and anion transference numbers are just

$$t_+ = \frac{m_+}{m_+ + m_-}, \quad t_- = \frac{m_-}{m_+ + m_-} \quad (1c)$$

under the monovalency assumption. In liquid electrolyte, one often finds interestingly that $t_+ < t_-$, despite the putative small size of Li^+ compared to anions like PF_6^- . This is because diffusion in liquid electrolyte occurs by the “vehicular diffusion” mechanism, where the entire solvation shell surrounding Li^+ needs to comove in the random walk, and Li^+ is often better solvated than PF_6^- , thus carrying a larger solvation shell. In contrast, in solid electrolyte like the SEI, there is $t_+ \approx 1$, since Li^+ moves by the “Grothuss” exchange mechanism as naked cation, completely different from that of vehicular diffusion. Larger solvent molecules like EC, DEC, DMC, ethyl–methyl

carbonates, etc., and PF_6^- , TFSI^- , FSI^- anions, are simply too large and cannot diffuse by the exchange mechanism in solid electrolytes.

Any discrepancy $c_+(\mathbf{x}) - c_-(\mathbf{x})$ induces net charge density in the liquid that triggers curvature in the electrostatic potential $\phi(\mathbf{x})$

$$e(c_+(\mathbf{x}) - c_-(\mathbf{x}))/\epsilon\epsilon_0 = \nabla \cdot \mathbf{E}(\mathbf{x}) = -\nabla^2\phi(\mathbf{x}) \quad (2)$$

where $e \equiv 1.60217662 \times 10^{-19} \text{ C}$, $\epsilon_0 = 8.854187817 \times 10^{-12} \text{ F m}^{-1}$, and ϵ is the dielectric constant of the pure solvent liquid (where there are bound charges and polarization but no free charge). Equations (1), (2) plus the Navier–Stokes equation for $\mathbf{v}(\mathbf{x})$ would close the equations.^[39]

We note that with a planar blocking anode, without $\mathbf{v}(\mathbf{x})$, upon applying a negative voltage on the anode ($x = 0$), the cation would be attracted whereas the anion would be repelled from the anode. This creates a positive space charge $c_+(\mathbf{x}) - c_-(\mathbf{x})$ and a negative curvature in $\phi(x)$, which is the well-known exponential screening curve, with width given by the Debye–Hückel length

$$\lambda_D \equiv \sqrt{\frac{\epsilon\epsilon_0 k_B T}{e^2 c_+^0 + e^2 c_-^0}} \quad (3)$$

where $e^2 c_+^0 + e^2 c_-^0$ is the ionic strength of the electrolyte before the field is applied. λ_D is of the order of 10 nm (note this is far below the optical observation lengthscale). However, once we let the cations to get across the SEI and get reduced (i.e., blocking \rightarrow nonblocking), in particular at high current densities, $c_+(x \rightarrow 0^+)$ will drop. This causes less screening of the applied negative voltage on the anode ($x = 0$), which will allow the electric field $\mathbf{E}(\mathbf{x})$ to penetrate deeper into the liquid electrolyte, that in turn will drive anions away from $x = 0$ that will cause even less screening. Countering this are the diffusional terms (first terms) in (1), which try to feed cations and anions back to the $x = 0$ region. However the strength of these terms decrease with time, since the diffusive fluxes becomes smaller and smaller with increasing diffusion depletion width $\propto (Dt)^{1/2}$ (if without convection), while the amount of lithium required in a galvanostatic experiment grows as $Q = It$, that increases linearly with time. The ionic strength of the electrolyte will decrease monotonically with time in front of $x = 0$, as the cations are captured and absorbed while the anions are driven away, allowing the electric field to penetrate deeper and deeper into the electrolyte. Once the local ionic strength $e^2 c_+(x = 0) + e^2 c_-(x = 0)$ drops to nearly zero (approaching “Sand’s extinction”), the working fluid turns from an electrolyte to a dielectric fluid, the electric field is not Debye–Hückel screened at all, and a sequence of long-range instabilities can happen.

When investigating copper electrodeposition in a mixture of copper sulfate and sulfuric acid, Sand found Cu^{2+} concentration went to zero (actually Nernst equilibrium concentration which is very low) near the electrode during Cu deposition, after which H_2 was generated. This shows U was able to drop further, indicative of approaching Sand’s singularity as the chemical potential of copper cation $\mu_+(x) \equiv \text{constant} + k_B T \ln \gamma_+ c_+(x)$ diverges quickly with $c_+(x \rightarrow 0^+) \rightarrow 0$.^[7] This model was then borrowed and extended to Li metal anodes at high current density, where the Li^+ concentration $c_+(x = 0)$ would be rapidly consumed and is expected to drop to zero at a finite time τ_s , and so will $c_-(x = 0)$.

This complete depletion of ionic strength near the electrode is known as Sand's extinction (turning electrolyte into a dielectric, and Debye–Hückel type screening to pure dielectric screening by ϵ) and the time τ_s is called Sand's time

$$\tau_s = \pi D \left(\frac{c_+^0 m_+ + m_-}{2J m_-} \right)^2 \quad (4a)$$

where J is the Faradaic current density and D is the ambipolar diffusion coefficient^[7]

$$D = (m_- D_+ + m_+ D_-) / (m_- + m_+) \quad (4b)$$

τ_s is simply the outcome of withdrawing cations from a diffusive region of width $\propto (Dt)^{1/2}$ (if without convection) with a constant drawing rate. Once τ_s is reached, there is no more Li^+ to be harvested by the first and second terms in (1a) near the electrode. Then the third term, which is mechanical motion and convection, must be activated if we keep galvanostatic drawing of the cations. One way to think about tip-grown dendrite (mode III)^[9] is that it is an attempt by the LMA to break out as an arm from the "extinction zone" $c_+(x) \approx 0$ and grab Li^+ from far out. The translational symmetry of the problem (planar geometry) has to be broken, because a planar front with quiescent fluid simply becomes too inefficient for transport after long enough time (τ_s). The situation is not unlike difficulties facing coastal fishermen who angle for a fish population in the ocean that does not reproduce.

It is interesting to note that if the anion transference number

$$t_- \equiv \frac{m_-}{m_+ + m_-} \quad (5)$$

is very small, then τ_s can be very long in (4). This is because if the anion moves very sluggishly, despite the pushing by the electric field, they move out very sluggishly, and therefore still stay as space charge, that will still lure Li^+ from afar that ameliorates the $c_+(x) \approx 0$ depletion problem.

The above assumes the anode is immersed in a semiinfinite fluid, and thus the diffusive width $\propto (Dt)^{1/2}$ (if without convection) can grow indefinitely with time. But if the fluid is sandwiched between the anode ($x = 0$) and a nonblocking cathode ($x = L$) that releases cations, then this imposes a truncation on

the how wide the depletion zone can become and how weak the recovery diffusions (first terms) in (1) can be, in which case a limiting current density

$$J^* = \frac{2ec_+^0 D}{t_- L} \quad (6)$$

is derived.^[8] According to this estimate, if $J < J^*(L)$ in a finite- L system, no mode III dendrite can ever form as Sand's extinction can never happen (even though other kinds of LMI can exist, such as mode I or II^[9]). But if $J > J^*$, Sand's extinction can occur within finite time even in a finite- L system, and it is possible to have genuine mode III tip-grown dendrite.

With a broad, planar LMA front, it was found experimentally that $v(x)$ would often exist near the LMA, with fluid electroconvection vortices that aid in the mixing of ions that breaks the 1D symmetry and favors the deposition of dendrites.^[38,39] In a capillary cell setup with a narrow LMA front, electroconvection is relatively suppressed, and so the Sand's time model more literally describes a limiting condition for Li dendrite formation and reveals the incubation time needed for Li dendrite growth is proportional to J^{-2} , as shown in Figure 2a. A drastic transition in LMI behavior was observed pre- and post-Sand's extinction. When applying a constant current, mossy lithium (modes I and II) starts to plate, leading to a decrease in the salt concentration near the surface; after a period ($t > \tau_s$) of polarization, there was a voltage divergence at the anode as the ionic strength depletes, and a wispy dendrite (mode III) shoots out very quickly in a tip-growing manner to keep itself in a finite ionic strength fluid region.^[12]

In general, Sand's time prediction is suitable for dendrite growth at a relatively high current density, $J > J^*(L)$, where L is the length between two electrodes.^[40] It shows that the marginal value of J^* is negatively related to the length between two electrodes, and that dendrite growth is easier in pouch cell than tightly pressed coin cells^[41] because of the larger distance between two electrodes. Recently, Bai et al.^[12] defined Sand's capacity (C_s) on the basis of Sand's time

$$C_s \equiv J\tau_s = \frac{\pi D}{J} \left(\frac{c_+^0 m_+ + m_-}{2 m_-} \right)^2 \quad (7)$$

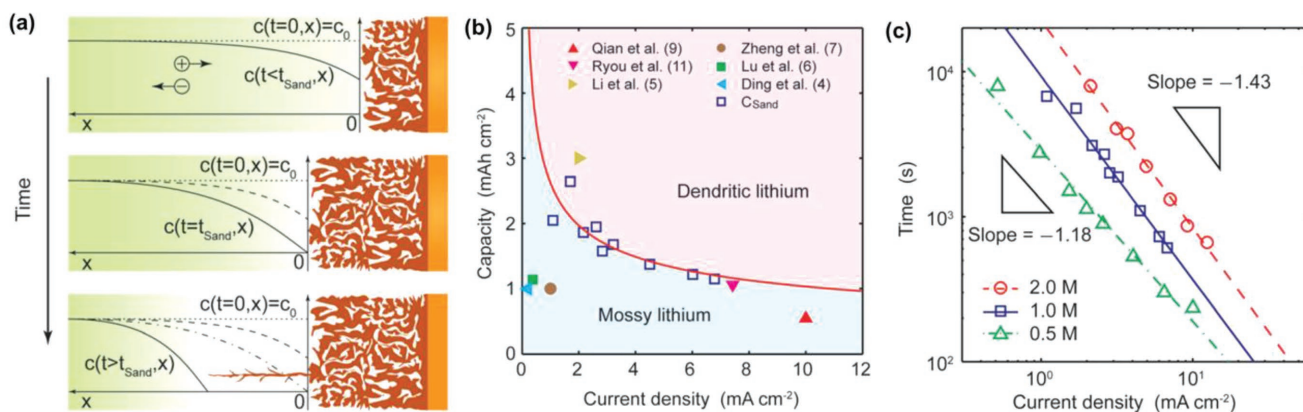


Figure 2. a) Lithium growth mechanisms during concentration polarization. b) Dependence of Sand's capacity on current density, which divides lithium growth mechanisms into mossy and dendritic regions at Sand's time. c) Concentration-dependent Sand's behavior. Reproduced with permission.^[12] Copyright 2016, Royal Society of Chemistry.

It was concluded that reaction-controlled mossy lithium are mostly extruded at the root and therefore could not pierce ceramic separator's nanopores due to the long distance between location of extrusion force and location of obstacle; while transport-controlled lithium dendrite grew at the tips and could thus easily follow the tortuous open pores like a heat-seeking missile, and penetrate the same separator to cause short circuit above Sand's capacity.^[22] The plot of Sand's capacity versus current density (Figure 2b) indicates a design principle to suppress tip-grown lithium dendrite (mode III), which are certainly more dangerous from the viewpoint of short-circuiting than mode II whisker and mode I mossy lithium (Figure 1b). From concentration-dependent Sand's behavior in Figure 2c, it was also found that highly concentrated electrolytes, with large ionic strength $e^2c_+^0 + e^2c_-^0$ and also lower anion transference number t_- , could largely raise the upper safety bound, which also verifies (at least from one aspect) why the high-ionic-strength "solvent-in-salt" electrolytes work so well.^[28,42]

Chazalviel^[37] predicted that lithium dendrite tips will grow at a speed that equals to "the velocity of the anions in the applied electric field."^[37] Brissot et al. observed that individual dendrites exhibit different velocities,^[8,40] which, nevertheless, are quite close to the velocity predicted by Chazalviel. In particular, they seem to be nearly in proportion to the current density. It is worth mentioning the driving force in those models is based on the electric field.

In the models above, the focus was on the liquid electrolyte. Capillary effect on Li atom chemical potential (Gibbs–Thomson/Ostwald–Freundlich effect) and the stress field development inside the BCC solid-phase lithium metal were ignored. So the lithium metal extrusion/deposition rate was treated too simplistically at the solid–liquid interface, a problem we have noted already in Section 1 with the stress generation mechanism due to SEI. Monroe and Newman then developed the first model to treat such solid-state stress effect, but with elasticity only. Instead of liquid electrolyte, they have chosen a solid electrolyte with a finite shear modulus and no inelastic relaxation (fracture or plastic deformation) mechanisms.

3.2. Stress and Inelastic Deformation Effects in the Solids

Monroe and Newman^[43] initially put forth "a propagation model for liquid electrolytes under galvanostatic conditions," where the effect of solid surface energy was evaluated, incorporating the solid tip curvature into dendrite growth kinetics. The Barton–Bockris method was adopted, taking into account the thermodynamic reference points and variable concentration as well as potential in the process of dendrite growth. Later, Monroe and Newman initiated a research to explore the influence of the elastic deformation of solid electrolytes on dendrite growth.^[44,45] Applying linear elasticity theory to a periodically deforming (elastic) lithium/electrolyte interface represented by a small sinusoidal perturbation, "the additional effect of bulk mechanical forces on electrode stability" was evaluated (Figure 3a), which indicated that an elastic modulus of the electrolyte/separator that was "twice that of lithium" was required to effectively prevent this sinusoidal perturbation from growing (since dense Li metal has a shear modulus of 3.4 GPa, one needs $E = 6.8$ GPa solid electrolytes, which point to ceramics-based

solid electrolytes).^[44,45] The key hypothesis of the Monroe–Newman model is linear elasticity, without inelastic stress relaxation mechanisms like plasticity or fracture, in either the Li metal or the solid electrolyte. A pre-existing tensile stress $\sigma(\mathbf{x})$ is assumed in the Li metal by the initial perturbation, namely, the lithium initially experiencing tension while the electrolyte initially bearing compressive stress (shown in Figure 3b). As an extended study where no protrusion was present at the electrolyte/lithium interface, namely a completely relaxed initial status (as illustrated in left part of Figure 3c), Barai et al.^[46] proposed a different scenario that compressive stress would occur in all three regions: the solid electrolyte, the newly formed lithium, and the original lithium substrate (illustrated as right part of Figure 3c) once lithium plating began. In this case, it was predicted that dendrite growth never happened at low current densities, independent of the elastic modulus of the electrolyte/separator.

The above discrepancy illustrates the importance of elasticity reference state, or the importance of specifying inelastic relaxation mechanisms, for modeling stress. It is well-known that while the stress can be well approximated by $\sigma(\mathbf{x}) = \mathbf{C}\boldsymbol{\epsilon}_{\text{elastic}}(\mathbf{x})$, where \mathbf{C} is the elastic constant tensor and $\boldsymbol{\epsilon}_{\text{elastic}}(\mathbf{x})$ is the elastic strain tensor, the definition of $\boldsymbol{\epsilon}_{\text{elastic}}(\mathbf{x})$ can be tricky, since only the total strain $\boldsymbol{\epsilon}_{\text{total}}(\mathbf{x}) = \boldsymbol{\epsilon}_{\text{elastic}}(\mathbf{x}) + \boldsymbol{\epsilon}_{\text{inelastic}}(\mathbf{x})$ is often specified by the boundary condition. With inelastic events such as plastic deformation, creep or fracture, with associated inelastic strain rate $\dot{\boldsymbol{\epsilon}}_{\text{inelastic}}(\boldsymbol{\sigma}, T)$ that also depends on the local stress, temperature and microstructure, a variety of different stress fields $\sigma(\mathbf{x})$ could result, that will bias the LMI evolution in different directions.

Recently, inelastic relaxation mechanisms in LMA such as fracture of the SEI, and plasticity of the lithium metal, have been considered. It has been shown that mode II root-grown metal whiskers of LMA^[9] have strong analogy with solid Sn whiskers seen extruding from Sn-based solders used in the microelectronics industry, as both Sn and Li are low-melting point metals and have appreciable atomic diffusivity even at room temperature.^[47] In both the Sn-based solders and LMA, a compressive stress can develop inside the low-melting-point metal. Subsequently, once a break occurs on the passivation layer on the surface, metal whiskers can be extruded out as a root-grown "atomic fountain," like a volcanic eruption through a fumarole.^[28] The whisker may maintain high crystallinity during such large mechanical deformation of extrusion. This is because Nabarro–Herring creep (metal lattice diffusion) or Coble creep (surface or grain boundary diffusion) mechanisms allow the solid to have extreme deformability^[48] at relatively low stresses, as long as the temperature is relatively high to enable these diffusive mechanisms.^[47] Dislocation plasticity is also possible in Li metal, at relatively larger stresses. From the fundamental studies of size-dependent plasticity,^[49,50] the diffusional creep and the dislocation slip mechanisms are predicted to have different size dependences. That is, with shrinking Li metal domain size, triggering dislocation slip will show "smaller is stronger" behavior, while triggering diffusional creep will show "smaller is softer" behavior. The stress relaxation mechanisms inside Li-metal is therefore a highly interesting problem scientifically, that depends on the spatial sizescale of the LMI and temperature. Coupling this with stress relaxation (plastic deformation and/or fracture) also going on inside the SEI, which is strongly

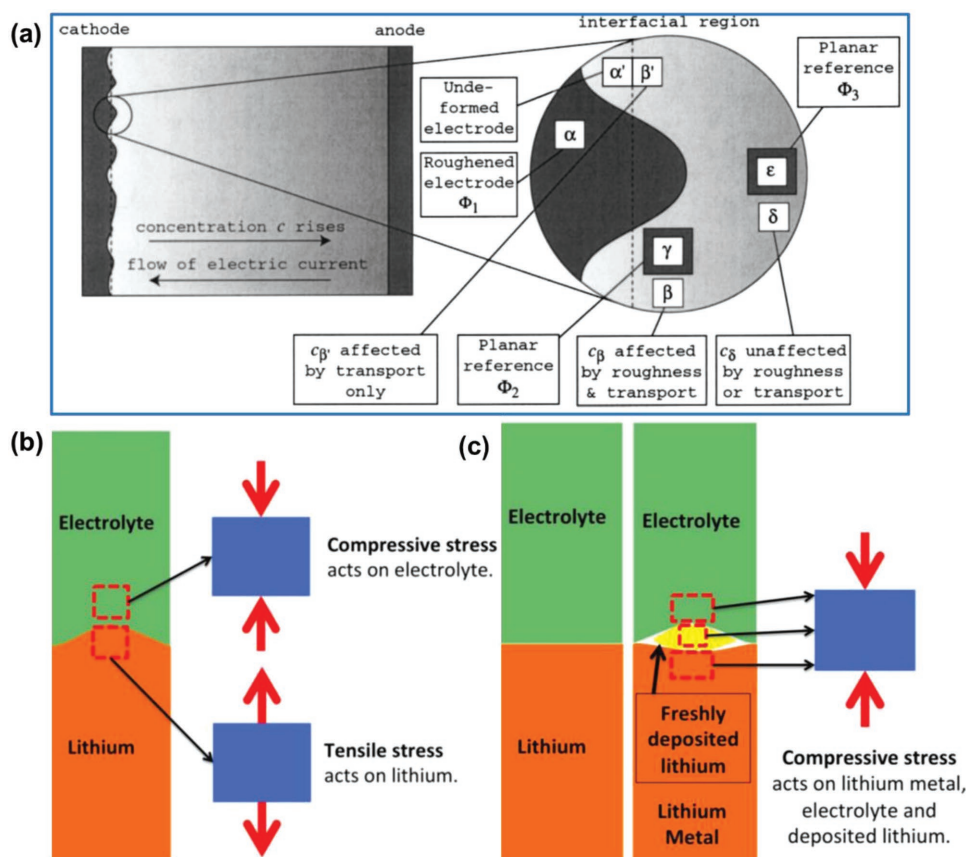


Figure 3. a) Diagram of a region near the tip of Li dendrites. Reproduced with permission.^[44] Copyright 2004, The Electrochemical Society. b) Schematic representation of the preapplied stress at the lithium/electrolyte interface in the Monroe–Newman model. c) Barai proposed relaxed initial state of lithium metal. b,c) Reproduced with permission.^[46] Copyright 2017, The Electrochemical Society.

stress-coupled with the Li metal, the scenario still needs to be worked out fully. Finally, we note that the internal stress field $\sigma(x)$ and boundary traction σ_{nn} are also coupled to the Li-atom chemical potential and equilibrium voltage of the half-cell Li/Li⁺ reaction as an electrochemomechanically coupled problem,^[51] so $\sigma(x)$ will certainly have an electrochemical overpotential signature, as the formation volume of BCC Li is $\Omega = 21.6 \text{ \AA}^3 \text{ atom}^{-1} = 0.135 \text{ eV GPa}^{-1}$.

An important application context of the above is designing thin aSEI or thicker solid electrolyte to effectively resist the growth of LMI during battery cycling. Although a shear modulus around 6.8 GPa of solid electrolyte is estimated to push the lithium dendrite back (based on dense lithium), which points to ceramics-based solid electrolytes, mossy lithium is often way softer than dense lithium ($E/E_{\text{ideal}} = (\rho/\rho_{\text{ideal}})^{3.6} = (1 - \phi)^{3.6}$, and take $\phi = 0.9$ here, we will get $E_{\text{mossy}} = 1.7 \text{ MPa}$), and therefore semi-solid electrolyte such as liquid–solid composite with only $\approx \text{MPa}$ level modulus, such as rubbery gels,^[15] may already provide sufficient mechanical back stress to suppress unrestrained ϕ -growth. However, since LMA cycling also has a long reach, the strain range needs to match, otherwise, “interface impedance” problem would occur, which was clearly present even with traditional polypropylene separators (Celgard 2400) which has $\approx 10^2 \text{ MPa}$ modulus and tens of percent of deformability.^[15] Rather than the traditional concept of “modulus bound,” we

believe that a different concept of “mechanical resonance,” namely an elastically soft ($\approx \text{MPa}$ modulus) but long-reach (several hundred percent deformability), elastomeric composite material that restrains porous lithium but never loses touch, could be a viable approach for managing porous lithium,^[15] instead of requiring GPa-level ceramic-based solid electrolyte. This 4S electrolyte approach could be combined with highly concentrated full-fluorine electrolytes to form semisolid gel electrolyte and enable highly reversible Li metal batteries.^[28]

3.3. Discrete-Agent-Based Models

Besides the continuum-scale conceptual and analytical models above, some discrete-agent-based numerical models have been developed to investigate the molecular mechanism of LMI. Among them, Mayers and co-workers developed a “particle-based coarse-grained (CG) simulation model” for the Li⁺ deposition, which helps to account for “heterogeneous and nonequilibrium nature of the electrodeposition dynamics.”^[52] In this model, cation electrodeposition is assumed to occur onto a hemispherical electrode and the counterion species are implicitly included with electrostatic screening. When plating with continuous charging, the deposition structure and trajectories reveal a strong dependence on the stochastic reduction

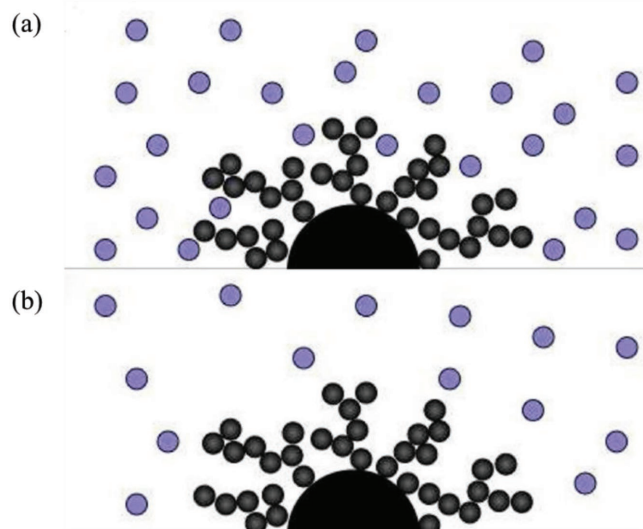


Figure 4. Schematic illustrations of the cation-diffusion dominated scenario and the reduction dominated scenario in CG model: a) cation-diffusion dominated scenario, and b) reduction dominated scenario. Reproduced with permission.^[52] Copyright 2012, American Chemical Society.

probability (akin to sticking coefficient in vapor deposition), and lower overpotentials generally correspond to more compact structures. The simulation of deposition trajectories indicates that dendrites came from a competition between timescales of cations diffusion during the deposition and cation reductive plating at the SEI/lithium interface. As illustrated in **Figure 4a**, when the conditions facilitate cation diffusion, Li^+ has a very deep

penetration into the deposition structure prior to its reduction on the structure, contributing to dense deposition structures and little lithium dendrite. Under conditions that favor cation reduction, timescales of reductive plating on the deposition structures are short and Li^+ reduction occurs before it penetrates deeply into the deposition structures (**Figure 4b**), leading to massive tip-grown lithium dendrite. Given the above-mentioned correlation between low overpotentials and compact structures, lower applied overpotentials promote cation diffusion and contribute to less propensity for dendrite formation, indicating that LMI would be suppressed with lower overpotentials. When using pulsed deposition, increasing γ ($\gamma \equiv t_{\text{off}}/t_{\text{on}}$) leads to decreased dendrite propensity since it extends the timescales of cation diffusion into the deposition structures.

Aryanfar et al. developed “a coarse-grained dynamical Monte Carlo (CG-MC) model.”^[53] Using “Monte Carlo simulations dealing with Li^+ diffusion and electromigration,” several pairs of pulse durations versus rest periods were evaluated, and an optimal pulse for dendrite inhabitation was estimated to be shorter than 3 ms, which corresponded to the relaxation time “for the diffusive charging of the electrochemical double layers” in the studied system.^[53] In a further CG-MC simulation, it was found that compared to the Li^+ mobility in the electrolytes, the mobility of interfacial lithium atoms dominated the dendrite morphologies (this is the aforementioned Coble creep mechanism^[47,48] for Li metal), which indicated that some approaches promoting lithium self-diffusion on solids would facilitate better control of dendrite growth.^[54] However, this model does not yet take into account the presence of the SEI. Recently, He and co-workers introduced all-atom molecular dynamics (MD) simulations^[55] to suppress LMI by applying rectangular cathodic pulses (**Figure 5a**). In their study, where the position

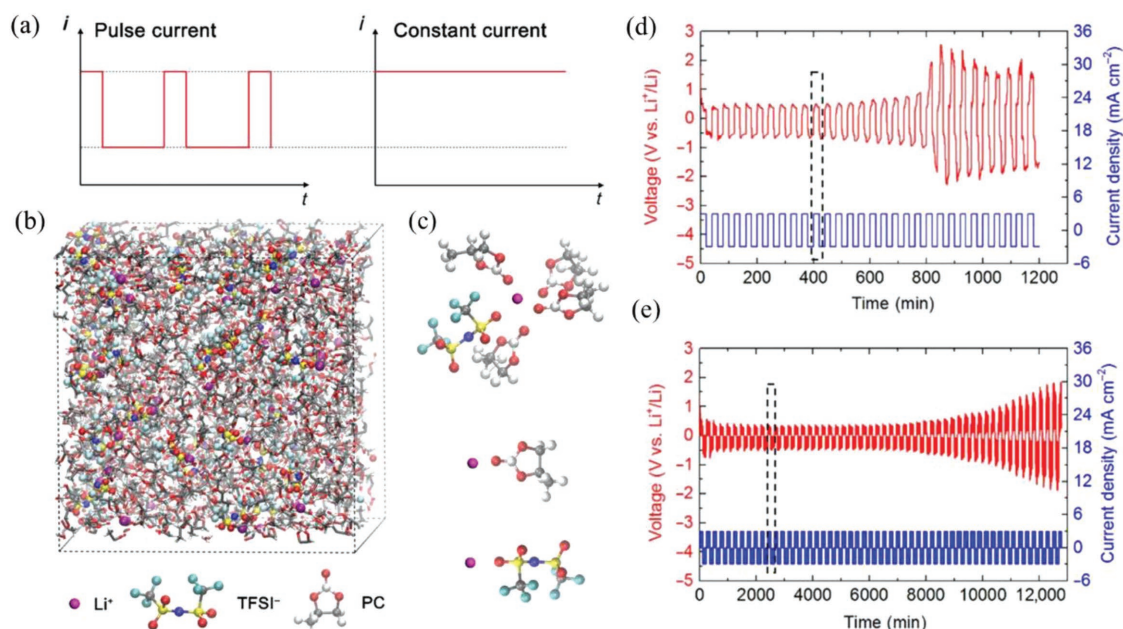


Figure 5. MD simulations of the electrolyte of 1 M LiTFSI/PC: a) Pulse current waveform (left) and constant current waveform (right). b) Snapshot of MD simulations. c) Representative configuration of Li^+ solvation used in MD simulations. d) Voltage and current profiles of Li symmetrical cells cycled with constant current at 3 mA cm^{-2} . e) Voltage and current profiles of Li symmetrical cells cycled with pulsed current ($t_{\text{on}}/t_{\text{off}} = 1:5$; $t_{\text{on}} = 1 \text{ s}$). Reproduced with permission.^[55] Copyright 2017, Science.

and velocity of each atom were modeled and the simulations were conducted in a cubic box (Figure 5b), the self-diffusion coefficient D of Li^+ was computed from mean square displacement of MD trajectories, which supports the notion that there exists an optimal γ ratio ($t_{\text{on}}/t_{\text{off}}$) for pulsed current charging in favor of Li ion inner diffusion to the utmost extent. Li^+ might combine with TFSI⁻ and PC, forming certain solvation structures (Figure 5c), but pulsed electric field weakens the association between Li^+ and TFSI⁻.^[55] The model confirms that low coordination number of TFSI⁻ around Li^+ is beneficial for Li ion diffusion. The cycle life of cells with pulsed current (Figure 5e) is much longer than that with constant current (Figure 5d) at the same current density.

3.4. Phase-Field Models

As mentioned in Sections 1 and 3.1, although the products of lithium electrodeposition in LMBs is usually called “lithium dendrites,” there are actually several growth modes: true dendrites (tip growth), whiskers (root growth), and “Eden cluster,” as illustrated in Figure 1b, or simply Li metal “arms” if we are not certain whether it was root-grown or tip-grown.^[9,12] In order to readily rationalize those patterns observed experimentally, phase-field models are developed to simulate the evolution of realistic microstructures during lithium deposition. Among them, Liang et al. proposed “a nonlinear phase-field model” to study “electrode/electrolyte interface evolution” during electrochemical reactions where the thermodynamic driving force was modified to reproduce Butler–Volmer kinetics as a function of overpotential in the sharp interface limit.^[56] Based on the principles of rate theory of chemical reaction kinetics, the Allen–Cahn equation was modified in their model to describe a nonlinear relation between the phase transformation rate and the thermodynamic driving force. Later then, Chen extended Liang’s nonlinear phase-field formalism to model lithium electrodeposition on electrode surface.^[57,58] In addition to the nonlinear phase-field equation describing motion of electrode–electrolyte interface, Chen also solved an ambipolar diffusion equation for Li^+ cations (see Equations (1),(2)) which included a reaction current term describing the asymmetry of the charge generation and depletion at the interface of electrode and electrolyte. Chen’s model predicted the formation and growth of lithium dendrite as a function of charge rate and qualitatively investigated the role of varying current density and rate constants on the deposition morphology. In order to systematically investigate the dendritic patterns, a range of applied voltage and protrusions was used to simulate dendritic growth. **Figure 6** shows three representative simulated electrodeposits with “fiber-like, fully dendritic” as well as “tip-splitting dendritic patterns” and a transition diagram of electrodeposition patterns with variable applied voltages and initial protuberant morphologies.^[57,58] When applying a relatively small voltage of -0.45 V and large b/a (a : diameter of dendrite, b : length of dendrite) value of 8.0, the typical pattern was fibrous branches, consistent with experimental observations. Also, a pattern transition from fibers to splitting tips were predicted through examining the phase diagram of applied voltage versus b/a : decreasing [overpotential] or b/a would facilitate a flat protuberant; for the

relatively large value of overpotential, there would always be splitting tip at the electrode–electrolyte interface.

Ely et al. developed the “asymptotic analysis of the phase field theory” with the incorporation of adhesion work, “interfacial electroplating,” and “electrolyte–dendrite interfacial energy.”^[59,60] Taking the interaction of electrodeposits into consideration, two distinct spatial regimes were identified during dendrite growth: (i) at the interface of current collector and lithium embryos where the growth kinetics was dominated by adhesion work and the stability of lithium was determined by the contact angles; and (ii) at the growth front of the arm where the competition between “the self-induced Laplace pressure” and the enhanced “electrochemical corner effect” influenced the lithium growth rate and dendritic patterns. As a result, a small contact angle would enhance the uniformity of electrodeposition layers while a large contact angle would accelerate Li arm detachment from the substrate, lower Coulombic efficiencies, and amplify deleterious side reactions. Recently, Jana and García^[61] performed more systematic research about the lithium dendrite growth mechanisms, and 5 regimes of behavior were identified: the “thermodynamic suppression regime,” the dendrite “incubation regime,” “the tip-controlled growth regime,” the “base-controlled growth regime,” and the “mixed growth regime.” They found “tip-controlled growth” linearly depended on time, while “base-controlled growth” was exponentially dependent on time.^[61]

While much of the modeling focused on Li metal deposition, the Li metal stripping dynamics thereafter is also extremely important, that should deserve more attention from the modelers. While mode III growth might be particularly bad for short-circuiting across the separator,^[12] Kushima et al. experimentally showed that mode II root-grown whiskers are particularly bad for CI and LMA reversibility. This is because with root-growth, the newly formed SEI at the root are thinner than the SEIs elsewhere. Thus when the current direction is reversed and Li metal is stripped, the impedance at root is lower and so the root might shrink faster than the tip. This eventually results in a hollow SEI stem at the root with no Li metal inside, and electrically disconnected dead lithium elsewhere in the arm. With a little bit of electroconvection in the fluid that stresses the stem, the whole arm can easily break off and fall into the fluid, generating lithium flotsams.^[9] This is why a white porous separator turns dark after Li metal-symmetric cell cycling, as these flotsams float around with the convecting fluid. The randomly stacked flotsams, a nanocomposite of porosity, gas, SEI and lithium metal, increases the nonlithium volume fraction ($\phi \equiv 1 - \rho/\rho_{\text{ideal}}$) and greatly exhausts the liquid electrolyte and cycleable lithium. They are also a safety concern (pyrophoricity, dust explosion) due to the large surface area. Since we now know mode II LMI is controlled by SEI mechanics, a way to ameliorate this particularly bad mode II irreversibility is to introduce more LiF into the SEI, which improves the mechanical properties of the SEI. Indeed, it was found that with increasing DFC, along with exponentially decreasing CI, the LMA morphology in SEM shows less and less number of long-aspect-ratio whiskers. With the ultraconcentrated, 7 M LiFSI-FEC full-fluorine electrolyte with DFC ≈ 17 , no long-aspect-ratio whiskers were seen at all even after many cycles, and the Li metal appears to deposit and strip as equiaxed grains. It would be interesting to model

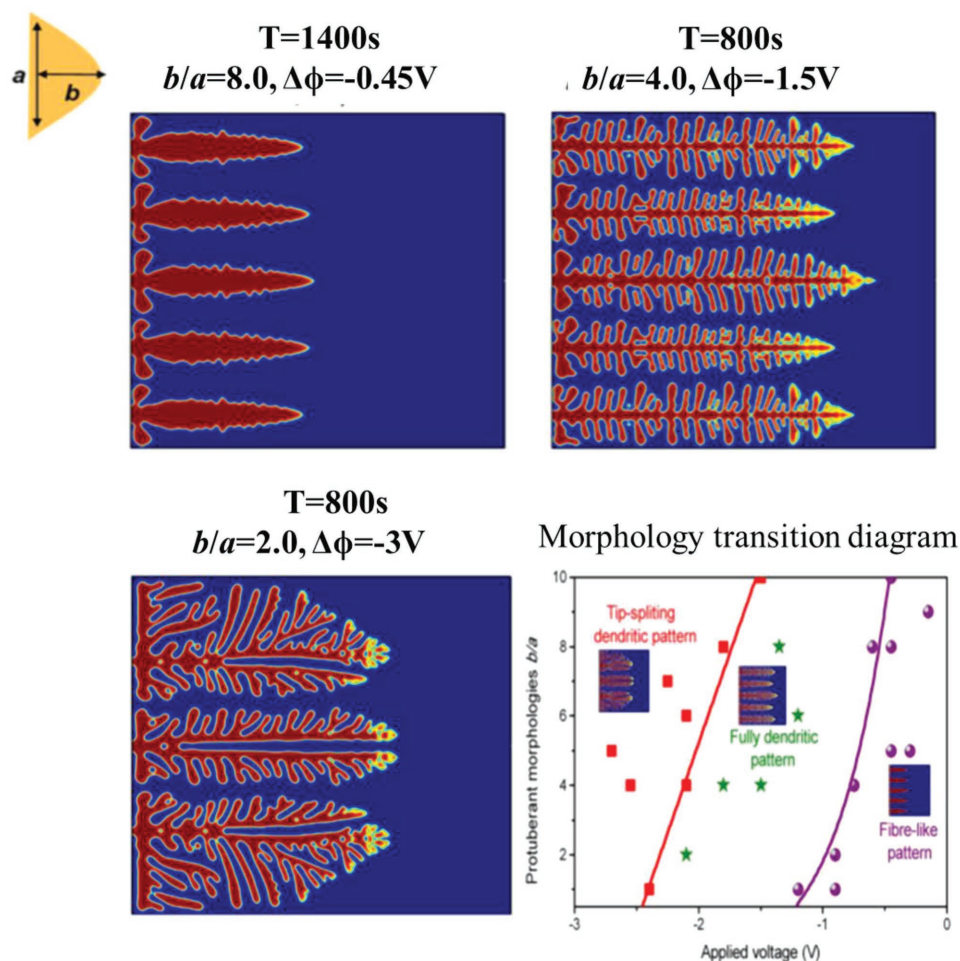


Figure 6. Three representative simulated electrodeposits with “fiber-like, fully dendritic” as well as “tip-splitting dendritic patterns” and a transition diagram of electrodeposition patterns with variable applied voltages and initial protuberant morphologies. Reproduced with permission.^[57] Copyright 2015, Elsevier B.V.

not just the first deposition and LMI, but stripping-redeposition for many follow-up cycles, and track the generation and compaction of lithium arms and flotsams.^[9]

4. Lithium Metal Protection

Although the analytical and conceptual models in Section 3 may not be perfect, they provide reference frames to explore the effect of electrolyte chemistry, surface status of electrodes and current density on LMI, which also guide the lithium metal protection research experimentally. A considerable number of methods have been proposed. Some LMA with dendrite-free morphology have been achieved under specific conditions. However, for getting LMB into mass-market, just a few bad failures in a million shipped units could have disastrous financial and societal consequences. The current LMAs are still not mature enough to be able to compete with graphite anodes, and perhaps Si-based anodes, on the mass market, and therefore more work in lithium metal protection is needed.

4.1. Electrolytes Optimization

In conventional Li-ion batteries, carbonates such as “PC, EC, DMC, and DEC,” are widely applied as the solvents of the liquid electrolytes.^[62,63] Despite their success in Li-ion batteries, the carbonate-based electrolytes (at least when they have dilute salt concentration, with low ionic strength) used to show severe deficiencies in LMBs in terms of Coulombic inefficiency, LMI, and cell life.^[20] Ether-based electrolytes exhibit more favorable LMI and Coulombic inefficiency when working with lithium metal,^[64] but their applications are restrained within a full-cell voltage window below 4 V because of the violent decomposition if $U_{\text{cathode}} > 4$ V versus Li/Li⁺. Although the electrochemical stability window of ether-based electrolytes is sufficient for lithium–sulfur batteries (the operating voltage ranges from 1.8 to 2.8 V), lithium metal versus TMO-type-cathodes work largely beyond 4 V, and therefore the energy density of full cells would be significantly limited.

As for the lithium metal anode, electrolytes with higher LUMO than the Li metal anode’s Fermi energy (μ_A) are traditionally considered to be desirable so they will not be consumed.

However, up to now, most of the studied polar aprotic solvents or lithium salt anions hold a LUMO below the Fermi energy of lithium metal.^[13,20,62] According to the solid-state stress and inelastic deformation models discussed above, the interface stability of SEI/lithium metal and ability of preventing LMI are largely affected by the mechanical properties of SEI, which depend on the electrolyte components (solvents, lithium salts, and additives), and therefore, it is reasonable to improve the SEI properties by optimizing the liquid electrolyte. Based on the dual-layer model of SEI films, although the mechanical strength is codetermined by the outer organic layer and inner inorganic layer, the shear modulus of the inorganic SEI is usually an order of magnitude higher than that of organic SEI,^[65] thus it is reasonable to assume that the mechanical properties are mainly influenced by the inorganic species of low oxidation states. Among those SEI components, LiF is believed to be an excellent passivation compound due to the reasons we mentioned in Section 2.1, and therefore high-DFC electrolytes, which largely encourage the formation of LiF-rich SEI, are usually good candidates. Also, at high salt concentrations, the large organic anion can be surrounded by one or more Li⁺ cations, forming contact ion pair (CIP, if an anion is in nearest-neighbor contact with one naked Li⁺) or aggregates (AGG, if an anion is in nearest-neighbor contact with 2 or more naked Li⁺),^[66] which lower the LUMO and HOMO energies of the

anion, making it easier to be reduced at the anode, while harder to be oxidized at the cathode. Energy-shifting effects also occur for the solvent molecules, who can now be surrounded by ions ("solvent-in-salt") rather than the other way around, changing their electrochemical stability window and also reducing their vapor pressure significantly (thus greatly reducing flammability, and improving safety). Recently, by using 7 M LiFSI-FEC electrolyte with DFC \approx 17, it was shown that the electrochemical stability window can be elevated to cover 5 V cathode, with excellent LMA reversibility and CI.^[28]

Generally, two strategies including fluorinated solvents and fluorine-abundant organic Li salts, are adopted to enhance DFC. For example, Markevich et al.^[67] studied the influence of FEC-based organic electrolyte on the performance of lithium metal anodes. It was demonstrated that, compared to the PC solvent, the FEC-based electrolyte (LiPF₆/FEC + DMC) exhibited a denser SEI layers on LMA and therefore better cycling performance of 1100 cycles even at a high current density of 2 mA cm⁻² and an area capacity of 3.3 mAh cm⁻², as shown in Figure 7b. Regarding the Li salts used in the electrolytes, an ideal electrolyte should possess high ionic conductivities and would also facilitate the formation of a stable SEI with high Li⁺ transference number.^[25,62] The most commonly used lithium salts LiPF₆ seems not suitable for lithium metal anodes, especially at high current density.^[64,68] Alternatively, LiTFSI and

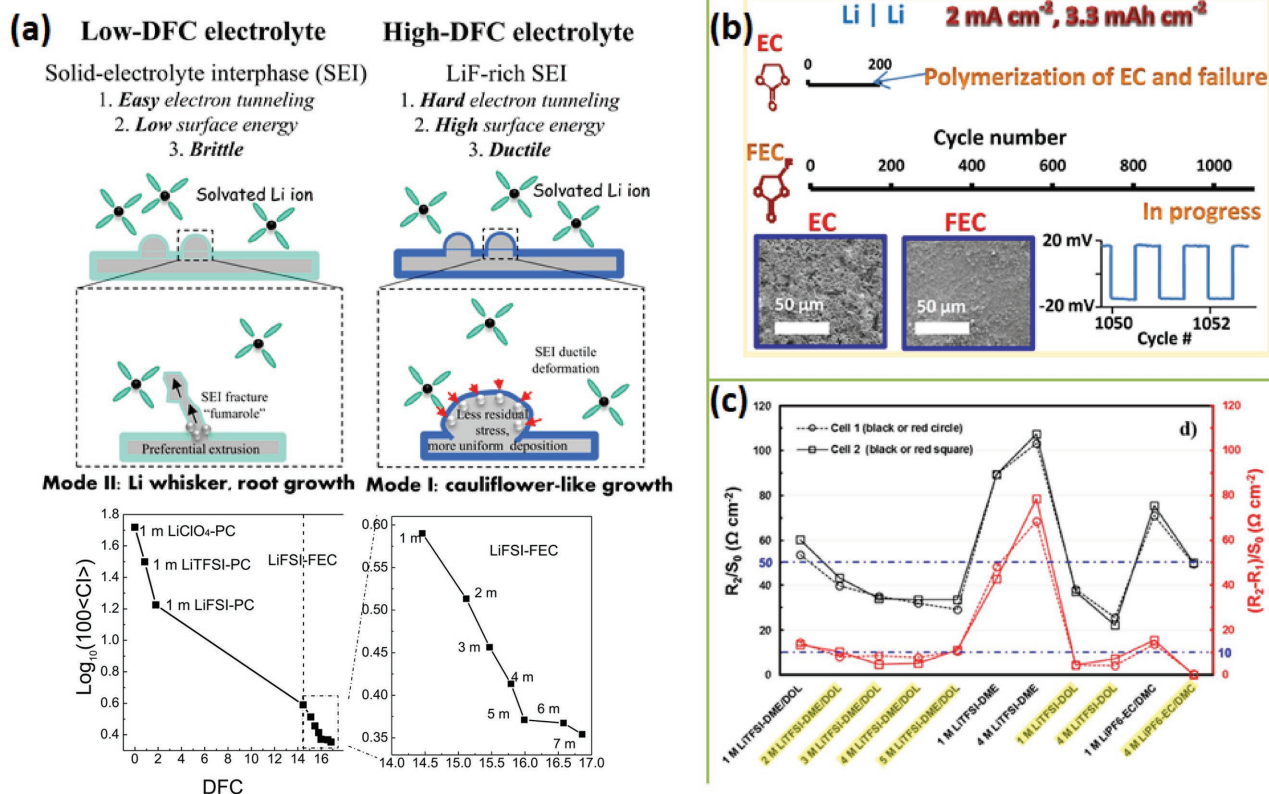


Figure 7. a) Schematic diagram of different Li growth mechanisms in low- and high-DFC electrolytes (upper); the exponentially decreasing relationship between CI and DFC (lower). Adapted with permission.^[28] Copyright 2018, National Academy of Sciences USA. b) Stable lithium metal stripping/plating at a current density of 2 mA cm⁻² and an areal capacity of 3.3 mAh cm⁻² in fluoroethylene-carbonate-based organic electrolyte solution. Reproduced with permission.^[67] Copyright 2017, American Chemical Society. c) Normalized resistance that indicates interaction between SEI and Li which could be mitigated depending on electrolyte/additive components. Reproduced with permission.^[74] Copyright 2017, Elsevier B.V.

LiFSI are two promising salts, with high dissociation constant, high-voltage stability, and good thermal and moisture stability.^[62] Especially, LiFSI-based electrolytes are beneficial for a compact and robust SEI layer to physically isolate the liquid electrolytes because of the relative affluence in active atomic F (higher DFC), as revealed in Figure 7a, and consequently, a whisker-free morphology was observed in Li metal cells using DOL/1,2-dimethoxyethane (DME)/LiFSI as electrolytes.^[68,69] As indicated in Figure 7a, electrolytes with full-fluorine solvent and high fluorine salt concentration promote the DFC and subsequently enhance SEI stability.^[70,71] Qian et al. developed a high concentration electrolyte of LiFSI in DME. With this electrolyte, lithium metal can achieve high Coulombic efficiency (up to 99.1%) during deposition/stripping without dendrite growth.^[68] Lately, the same group identified that a richer-LiF and denser SEI were formed in 4 M LiFSI-DME than those formed in the 1 M LiFSI-DME by a multinuclear “solid-state MAS NMR study at high magnetic field.”^[72] Suo introduced an even higher concentration of lithium salts, namely, “solvent-in-salt” electrolyte, to effectively suppress lithium dendrite in LMBs owing to the abundant “anion to keep the balance of cation (Li⁺) and anion (TFSI⁻) near metallic lithium” anodes, to prevent the depletion of ionic strength and the onset of Sand’s singularity.^[42] Recently, Suo developed a new kind of superconcentrated fluorine-donating electrolyte (7 M LiFSI/FEC), where both the solvent and the salt donate F, and using this electrolyte, lithium anode porosity was significantly suppressed and the CE was promoted to 99.64%, the best CE of lithium metal ever reported in 5 V class battery at such areal capacity and rate.^[73]

Another factor that needs to be considered when optimizing electrolytes is Li⁺ transport properties. Through electrochemical impedance spectroscopy, Xiao found that while the electrolytes constitution could modulate the resistance of nSEI layer as demonstrated in Figure 7c, there seems to be conflicting requirements in Li⁺ transport, namely low impedance (thin nSEI) would increase the propensity of breakage and “flooding,” while high impedance (thick nSEI) would decrease cell power and dry out the electrolytes.^[74] Extending this concept to aSEI, while a thick but 4S electrolyte may never break, if the Li-ion resistivity is too large, it may not be useful. An optimal thickness for the aSEI therefore exists.

In addition to conventional organic liquid, ionic liquids also hold great promise for lithium metal anodes due to “its wide electrochemical window, high conductivity, high thermal stability, low safety hazards” (nonflammable, nonvolatile), and low toxicity.^[75,76] For example, Guo and co-workers utilized “hybrid *N*-propyl-*N*-methylpyrrolidinium bis(trifluoromethanesulfonyl) amide (Py₁₃TFSI) and ether electrolyte” to passivate lithium metal, which was found to largely stabilize the SEI layer, and therefore efficiently restrained LMI during cycling of LMBs.^[75] Wang et al. also reported the stable plating/stripping cycles with a high areal-capacity (12 mAh cm⁻²) and excellent Coulombic efficiency (>99.98%) at high current densities (>5 mA cm⁻²) when utilizing low-concentrated solvated ionic liquid (LiFSI/tetraethylene glycol dimethyl ether (G4) + DOL).^[76]

While fluorinated solvents and salts and fluorine-containing room-temperature ionic liquids have shown significant advantage in promoting better nSEI and reducing volatility and flammability, they tend to be quite expensive today due to special

concerns in fluorine chemistry processing. Phosphate-based electrolytes have also shown good flame-retarding properties, and recently it was shown they can be produced scalably with 100% atom economy (no byproducts or need for purification),^[77] opening the way for large-scale production.

4.2. Electrolyte Additives

Besides the design of solvents and lithium salts, modifying electrolytes with additives has been considered another strategy to enhance the performance of lithium metal anodes,^[22,25,62] as it was found that only a small concentration of additives could enhance the battery performance or safety tremendously. A great variety of additives have been found to work to a degree with lithium metal, and in most cases, electrolyte additives are designed to be sacrificial to promote the formation of stable SEI during the initial activation cycles of LMBs and subsequently prevent exhaustion of cycleable lithium, solvent or salt anions in the following cycles.

Typically, a good electrolyte additive should have a lower LUMO to ensure the more preferential reduction reactions than Li salts and solvents in the electrolyte.^[13] FEC was a classic electrolyte additive in high-energy-density LMB to protect a Li metal anode,^[78] with a very low LUMO level of -0.87 eV by first-principles calculations and therefore easily reduced to form LiF on the surface of Li metal anodes. Such LiF-rich SEI is believed to be advantageous in suppressing LMI and improving Coulombic efficiency. A measure of generalized donatable fluorine concentration (GDFC) may be proposed, where any other electrolyte components besides F atom involved that could improve SEI performance like LiF, mechanically or electrochemically, are included. GDFC could be used to quantify a lot of other electrolyte additives. For example, Al₂O₃-rich SEI layer was also proved to be mechanically superior in suppressing lithium dendrite:^[79] through a controllable introduction of AlCl₃ to electrolyte, it is demonstrated that a reaction of AlCl₃ with trace water in the electrolyte was initiated to generate a mechanically and chemically stable Al₂O₃ in the SEI layer on the lithium surface. Due to the high mechanical strength of Al₂O₃, mode II lithium whisker growth was effectively suppressed during lithium plating and stripping. Moreover, “AlCl₃-based positively charged colloidal particles” could be formed in the electrolyte, which worked as electrostatic shields around the protrusive lithium during the plating process and guided the following deposition of metallic lithium to the vicinity of the protruding Li, just as the mechanism of self-healing electrostatic shield proposed by Ding et al.,^[80] shown in Figure 8a.^[79] Similarly, inspired by the industrial electroplating techniques that adopt nanodiamonds as an electrolyte additive, Cheng significantly improved the mechanical and electrochemical performance of as-derived SEI layer and therefore suppressed the growth of LMI.^[81] First-principles calculations indicated that lithium preferred to adsorb onto nanodiamond surfaces with a low diffusion energy barrier, thus leading to uniformly deposited lithium arrays.

In addition to constructing a high-performance SEI film through GDFC, another protection mechanism could be derived from the models (Section 3) which indicated a lower overpotential would contribute to a more compact electrodeposition layer. For example, Choudhury reported an in situ electroless

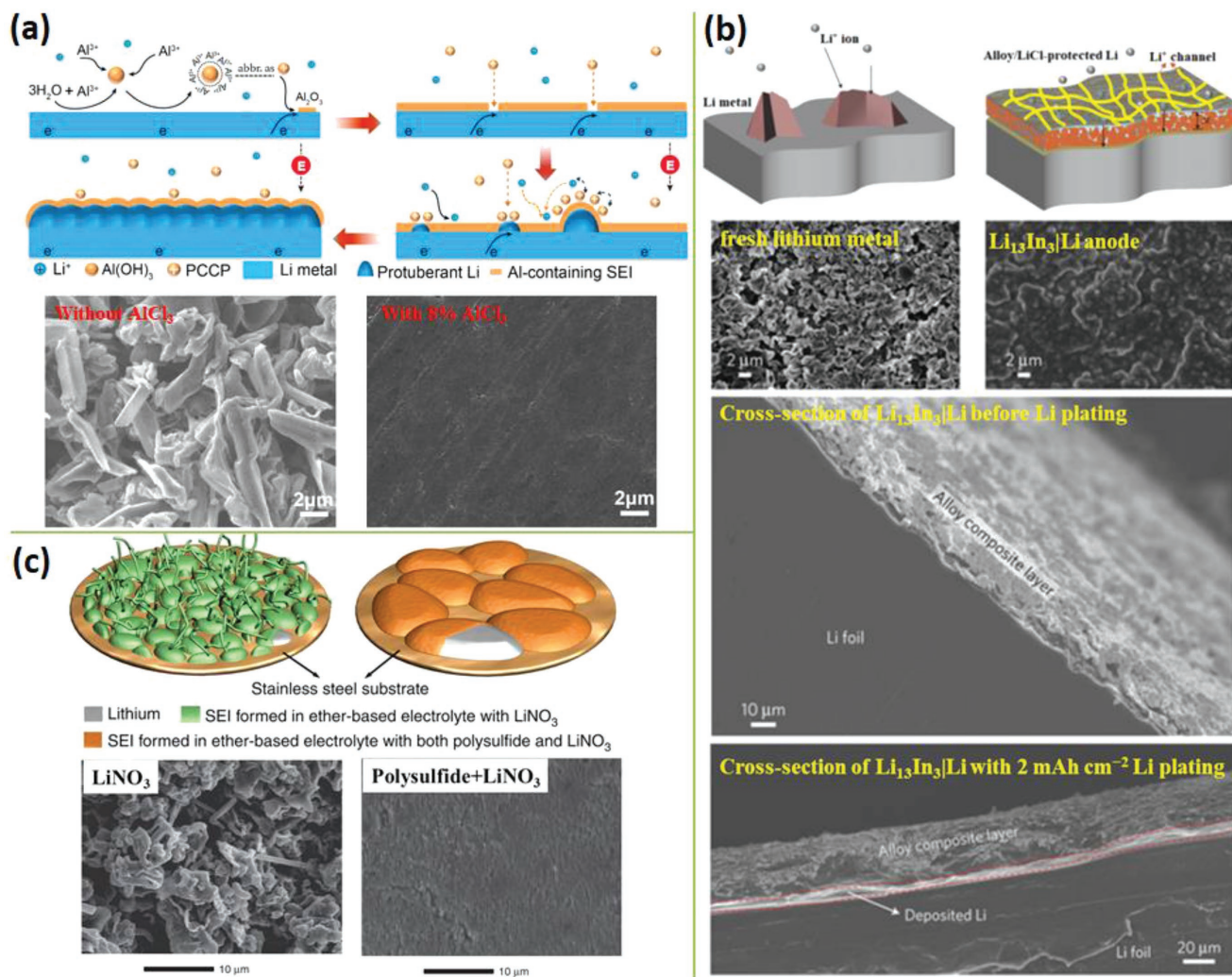


Figure 8. a) Schematic illustration of the lithium deposition process in the AlCl_3 -added electrolyte. Reproduced with permission.^[79] Copyright 2017, Elsevier B.V. b) Schematically illustrating the working mechanism of alloy-protected lithium anodes. Reproduced with permission.^[83] Copyright 2017, Nature Publishing Group. c) Schematic diagrams describing the ion diffusion channels in the (left) routine and (right) sulfurized SEI films. Reproduced with permission.^[85] Copyright 2015, Nature Publishing Group.

plating technique to coat indium on lithium metal, and faster surface transport of lithium was facilitated, thus beneficial for forming more uniform Li electrodeposits (by Coble creep relaxation,^[47,48] Section 3.2).^[82] Besides, the interfacial resistance of the resultant In–Li hybrid electrode was significantly lower than that of the pristine Li metal which indicates the indium metal coating could protect the lithium metal effectively. Another successful demonstration was made by Nazar and co-workers, who directly reduced metal chlorides at the lithium anodes to in situ generate surface layers comprised of Li_xM alloys (M could be In, Zn, Bi, or As) in which lithium diffused much faster than in metallic lithium,^[83] again taking advantage of Coble creep relaxation.^[47,48] Additionally, the insulating nature of the LiCl in the Li_xM alloy also guarantee lithium deposition under the protective alloy layer instead of reduction on the surface (Figure 8b). Although soluble lithium polysulfides has been viewed as a key obstacle for Li–S battery cathode,^[29,84] synergistic interactions of Li_2S_8 , LiNO_3 and lithium metal were utilized to

build a highway of Li^+ transport on the parallel direction to lithium anodes.^[85] By manipulating the concentration of LiNO_3 and Li_2S_8 in the electrolytes, the Coulombic efficiency and cycle life of the LMBs were greatly improved, “with Coulombic efficiency maintained at 99% for over 300 cycles at 2 mA cm^{-2} ” and no obvious lithium dendrites formed “up to a deposited lithium capacity of 6 mAh cm^{-2} .”^[77] It was proposed that the sulfurized SEI could be achieved by the direct contact of fresh Li metal with a lithium polysulfide (Li_2S_x)–lithium nitrate (LiNO_3)–lithium bis(trifluoromethanesulfonyl) imide (LiTFSI) electrolyte, which provided more channels for Li-ion diffusion thus increasing the ionic conductivities (Figure 8c).^[85,86]

4.3. Artificial SEI and Soft Solid Electrolyte Structure

Although optimizing liquid electrolytes is a convenient approach to protect lithium metal anode and significant progress

has been achieved in the past decades, there are still great challenges for commercialization of LMBs in liquid electrolytes. For example, for the next generation energy-dense lithium metal batteries, more than 4 mAh cm^{-2} areal capacity of LMA is required. For lithium–sulfur batteries, the average working voltage is 50% lower, so the areal capacity of lithium metal anode should be at least 5 mAh cm^{-2} , or at least $25 \mu\text{m}$ thick if fully dense. However, the plating/stripping areal capacity of lithium metal in the electrolyte study is usually lower than 3 mAh cm^{-2} , and lithium metal still suffers from serious electrolyte corrosion and pulverization at higher current density. The main reason, we believe, is in situ formed SEI films (both nSEI and aSEI) typically are well adherent to lithium substrates, and therefore repeated large dimensional changes would inevitably cause fatigue fracture in such SEI films even if specially designed. Therefore, an ex situ aSEI which is weakly-/non-clinging to lithium could provide more effective protection. This philosophy was firstly demonstrated successfully by Cui and co-workers, who fabricated interconnected hollow carbon nanospheres on Cu current collectors, as illustrated in Figure 9a. When lithium deposition started, this layer with a high ion conductivity and stable electrochemistry would be pushed out (Figure 9b) but still protecting the freshly obtained lithium underneath, which enabled the “Coulombic efficiency of 99% for more than 150 cycles in Cu|Li cells” (Figure 9c).^[87] Furthermore, Zhao reported using 2D h-BN, which stopped electrons but not Li^+ ions (high t_+ and is therefore aSEI), as the protecting layer. It was found through first-principles calculations that due to the interlayer spacing of 2D h-BN, the adsorption energy is higher than that provided by bare Li or h-BN layer, which contributes to uniform lithium deposition under h-BN layer.^[88]

Ultrasoft (elastic modulus less than 50 MPa, three orders of magnitude softer than the Monroe–Newman modulus bound of 6.8 GPa, Section 3.2), semisolid electrolyte with a “mechanical resonance” structure that restrains LMA but never loses touch could provide low impedance and efficient lithium protection.^[15] Therefore, viscoelastic polymer electrolyte layers that can keep adhering to current collector or lithium metal tightly (4S electrolyte,^[15] not “brittle” nSEI) were developed. For instance, a protective layer consisting of polyacrylonitrile (PAN) fiber array was designed by Wu.^[89] Under the templating of such PAN arrays, uniform lithium deposition was shown, and the average CE of lithium metal anode sustained 97.4% “for 250 cycles at a current density of 1 mA cm^{-2} .”^[89] Other polymers such as a PDMS film^[90] have also been explored to suppress the dendrites and accommodate volume variation, but an inevitable issue that should be addressed concerning polymers is the insufficient lithium ion conductivities. In this context, the polymer/inorganic hybrids were then brought to attention. A typical example is garnet/poly(ethylene oxide)-based polymer hybrid ion-conducting protective layer reported by Hu, who dispersed garnet-type $\text{Li}_7\text{La}_3\text{Zr}_{1.75}\text{Nb}_{0.25}\text{O}_{12}$ powders into mixed solution of PEO and LiTFSI, and then cast the suspension onto lithium metal. In this case, modified lithium metal anode would plate more uniformly under the protective layer and the CE could be up to 99.5% after 1000h.^[91]

4.4. 3D Electrode Frameworks

Besides thin artificial SEI, and thicker but 4S electrolyte, another design to suppress lithium dendrite is to lower the

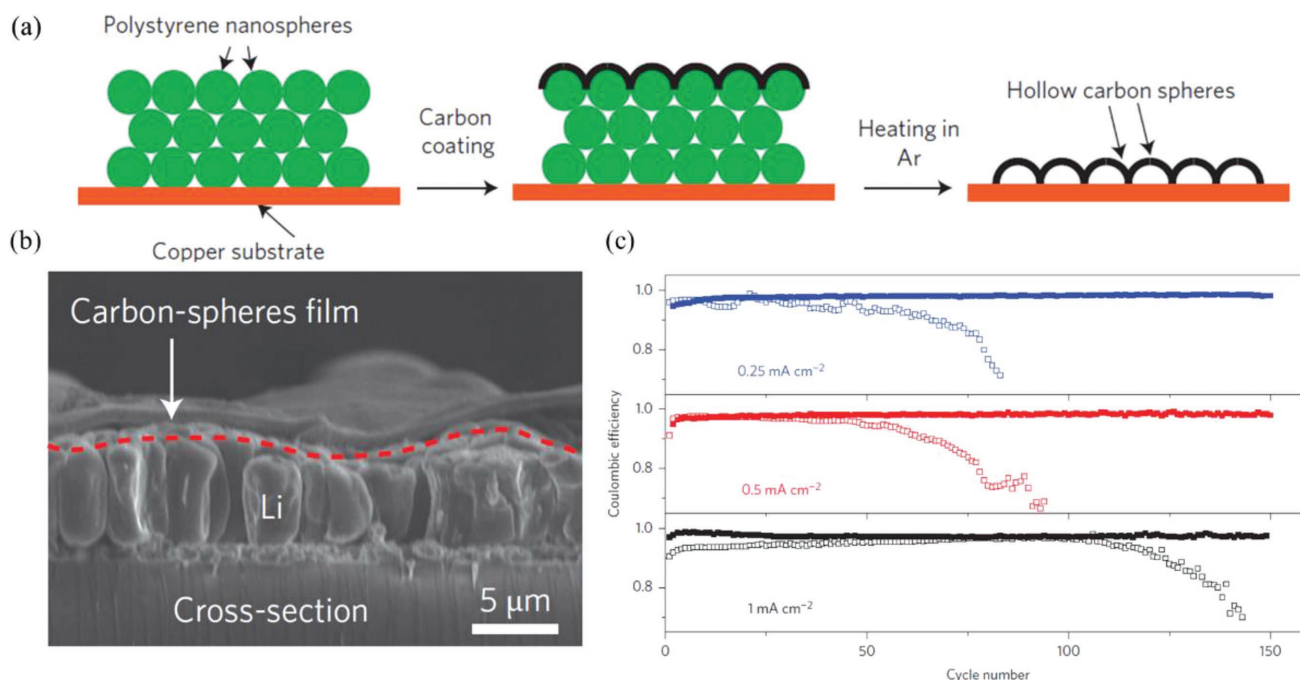


Figure 9. a) Schematic diagrams of fabrication steps of the modified Cu electrode by hollow carbon nanospheres. b) Cross-sectional SEM image after lithium deposited between the carbon-spheres film and the Cu substrate. c) Cycling performances of the modified Cu electrode by hollow carbon nanospheres (solid symbols) and the bare Cu substrate without modifications (hollow symbols) at various current densities. Reproduced with permission.^[87] Copyright 2014, Nature Publishing Group.

current density, as discussed in Section 3.1. A straightforward approach is to increase the surface area of the electrode to reduce the current density. Along this line of thought, various current collectors, including “3D current collectors with a sub-micrometers skeleton,”^[92] 3D porous copper current collector vertically aligned microchannels,^[93] and free-standing copper nanowire network^[94] to accommodate the volume expansion and lithium dendrite growth during cycling, have been applied to host the Li metal through an electrodeposition approach. As shown in **Figure 10a**, for planar Cu current collector, the growth of Li at limited areas is accelerated due to high local electric field. In contrast, the interconnected CuNWs with high surface area can significantly decrease the Li-ion flux, and thus more

uniform lithium deposition can be achieved on the macroscale. Especially, once a few dendrites come up, they would be confined inside the interconnected network and form bulk Li instead of needle-like lithium. With the free-standing CuNWs network current collector, lithium metal can stably work for 200 cycles and keep average CE up to $\approx 98.6\%$ (Figure 10b).^[94]

3D current collectors other than copper were also developed to serve as a “cage” for the lithium redeposition in order to accommodate the infinite-percentage volume expansion. For example, grooves of micropatterned Ti foil were prepared by focused ion beam carving technique to ensure a preferential deposition of the Li metal. Consistent with the lightning rod theory of classical electromagnetism, electrolytes

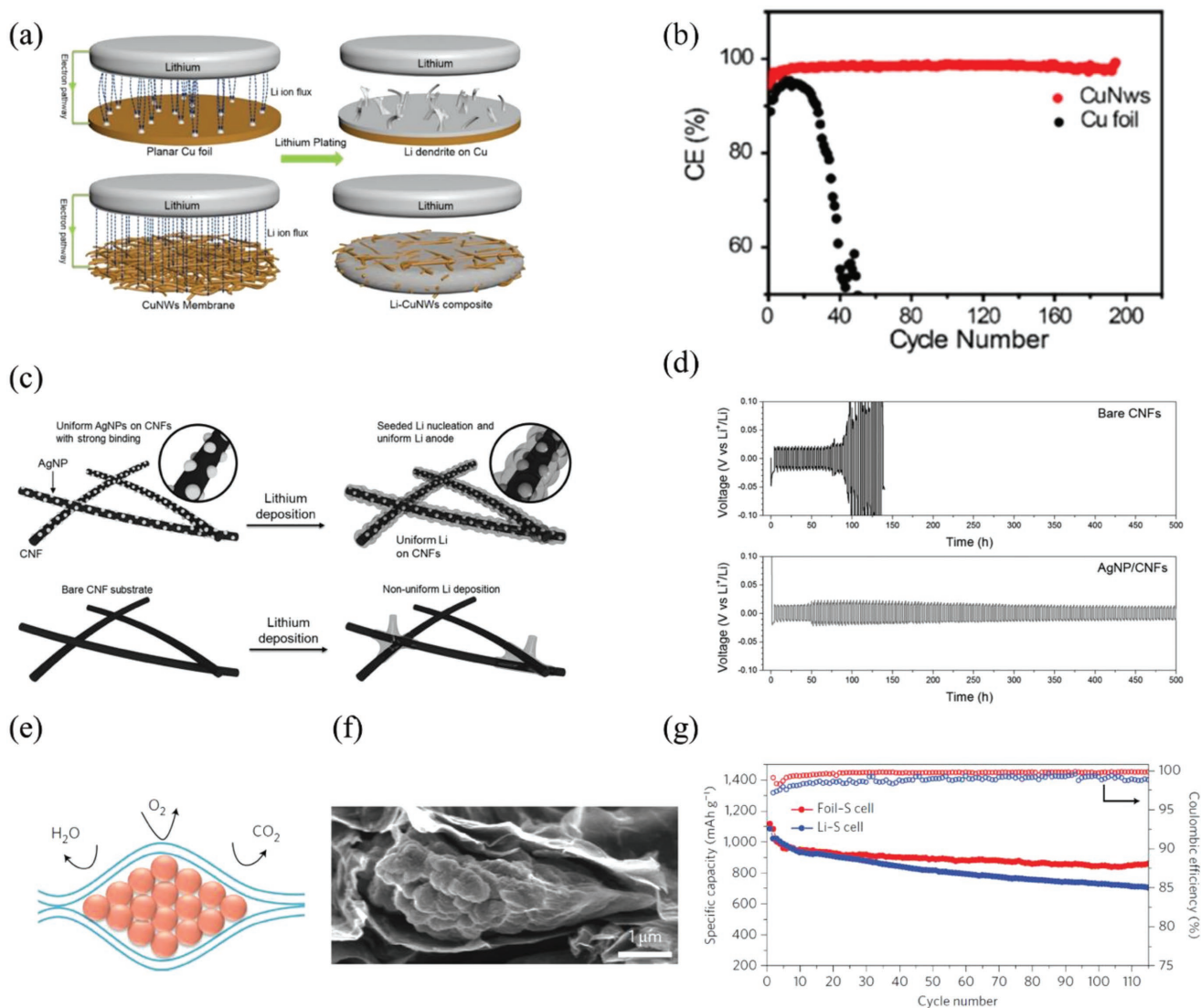


Figure 10. a) Schematic illustration of plating models of metallic lithium on the planar Cu current collector and the Cu NW current collector. b) Coulombic efficiency and cycling performance of two different current collectors. a,b) Reproduced with permission.^[94] Copyright 2016, American Chemical Society. c) Schematic illustrations of AgNP-anchored CNF substrate as a 3D host for homogeneous deposition of lithium metal (upper part) and Li deposition on bare CNF substrate without AgNPs (lower part). d) Cycling performance of bare CNFs and AgNP/CNFs composites. c,d) Reproduced with permission.^[99] Copyright 2017, Wiley-VCH. e) Schematic illustration of Li_xM/graphene composites that are air-stable. f) Cross-sectional view of Li_xSi clusters well encapsulated by graphene. g) Cycling performance of lithium-sulfur batteries with Li_xSi/graphene composites and bare lithium foil respectively as anodes at a rate of 0.5 C. e-g) Reproduced with permission.^[101] Copyright 2017, Nature Publishing Group.

in the grooves show a tip effect, resulting in a stronger electric field in the grooves that attracts a larger Li-ion flux, and therefore lead to lithium depositing in the grooves preferentially.^[95] Besides, some other high-surface-area carbon-based materials were also reported as 3D current collectors, such as “a scaffold made of covalently connected graphite microtubes,”^[96] carbon nanofibers.^[97] However, since extra nucleation overpotential is required to plate lithium on the carbon matrix,^[98] those lithium ions without enough driving force would prefer a direct deposition on the surface instead of filling the pores. To mitigate this, “seeds” are usually planted inside to induce the lithium deposition. For example, a composite structure of silver nanoparticles (AgNPs) attached on carbon nanofibers (CNFs)^[99] was fabricated, which exhibited a more homogeneous Li nucleation (Figure 10c) and a better cycling stability (Figure 10d) compared to bare CNFs substrates. A similar design principle was also demonstrated in a “bamboo-derived” 3D hierarchically porous carbon “decorated by ZnO quantum dots” (ZnO@HPC).^[100] The lithiophilic ZnO nanoparticles seeded in the porous carbon can induce lithium deposition uniformly as well as provide rich and homogeneous nucleation sites for lithium deposition. Thus, lithium prefers to plate on ZnO rather than porous carbon.^[100] Especially, compared to lithium foils, ZnO@HPC connected by 3D hierarchical porous carbon scaffold with quantum ZnO dots guides lithium deposition more uniformly, as an innovative way to build 3D frameworks. A well-designed 3D electrode framework is a strategy to kill two birds with one stone: the hosts not only provide free space for prestored metallic Li (prelithiation) and receiving fresh Li ions in later cycling, but also induce uniform Li plating/stripping in the designed framework, which consequently guarantee a minimum apparent dimensional change and an effective dendrite trap. However, prestoring Li through an electrodeposition approach (prelithiation to achieve “0.5 × excess,” “1 × excess,” “1.5 × excess,” etc. in Section 2.3), which currently requires assembling the 3D host and sacrificial bare Li foil into a working cell first, generally causes uneven Li deposition considering that Li metal mostly prefers to plate on the top of the 3D host network because of a shorter Li-ion diffusion pathway. Moreover, one has to later disassemble this and carefully clean the resultant 3D electrode to completely remove the residual Li salts and electrolytes from the prelithiation, resulting in tedious electrode fabrication process and is probably unrealistic for practical applications.

To further improve the scalability, researchers developed prelithiation methods other than electrochemical deposition, through infusing molten Li into the 3D porous nanostructure. Such design concept was well embodied in an air-stable lithium alloy/graphene foil by Cui and co-workers, who fabricated large-scale and free-standing Li_xM/graphene composites with densely packed active Li_xM nanoparticles fully encapsulated by graphene sheets (Figure 10e).^[101] As the fully swelled Li_xSi was well constrained in the graphene cage (Figure 10f), the composite got rid of the critical issues of volume expansion and LMI that keep consuming active Li, to ensure a good cyclability (Figure 10g).^[101] Another example was demonstrated in the Li–Ni composite electrode, where the metallic Ni foam is employed as a stable host for prestoring Li via thermal infusion.^[102] Based on the analysis of

Li stripping/plating behavior of Li–Ni composite, the Ni foam host not only works as a framed cage for lithium metal, but also effectively accommodates the surface tension generated by the Li–Ni composite during cycling, thus preventing lithium dendrite growth and restricting the thickness variation of Li anodes ($\approx 3.1\%$).^[102]

5. Dynamic Characterizations of Lithium Metal Anode

Ex situ characterization techniques have been developed to facilitate fundamental understanding of LMI. However, the complexity of constantly changing electrochemical environment has limited information extracted to a large extent, until the availability of diverse in situ characterization techniques. Real-time optical and X-ray, scanning and transmission electron microscopies of electrochemical behaviors are the most significant technological breakthroughs recently that enable the dynamic visualization of LMI (Sections 2 and 3) and in-depth understanding of the LMA protection mechanisms (Section 4) in the past decade.^[103]

5.1. In Situ Optical and X-ray Microscopy Techniques

In situ optical microscopy techniques are powerful tools for observing LMA plating/stripping processes in working conditions that could mimic practical applications.^[104] It consists of an optical microscope, a CCD camera, a visual cell (the most important part) and a current meter to dynamically monitor the batteries. The systems can be classified into many categories, for example, three-electrode or two-electrode systems depending on the different electrode system of visual cell. Dendrite formation can be identified instantaneously and facilely, and therefore are widely applied in the study of lithium metal anodes. As shown in **Figure 11a**, Bai et al. put lithium metal symmetric cells in the glass capillary and visualized LMA’s microstructural evolution. They unraveled a mechanism transition from mode I “mossy lithium” growth to mode III true dendrite growth at tips, at Sand’s time (Figure 11b)^[12,15] discussed in Section 3.1. Furthermore, in sandwich cells, they further demonstrated that while dendritic lithium could easily pierce through nanopores to cause a short circuit, nanoporous ceramic separators were able to block mossy lithium. Meanwhile, through in situ observations of capillary cells, Li and co-workers^[15] also found lithium metal penetration was suppressed by a rubber separator much softer than 6.8 GPa suggested by Monroe–Newman limit for solid electrolyte (Figure 11c), indicating that the elastomeric 4S (soft, stretchy and sticky solid) electrolyte was an excellent choice for accommodating large volume change of Li anodes, while maintaining a low contact impedance like a self-stressed Li metal balloon.

Recently, based on the conventional in situ optical microscope equipment, more advanced multifunctional techniques are developed. For instance, X-ray nanocomputed tomography was incorporated into in situ optical microscopy to investigate

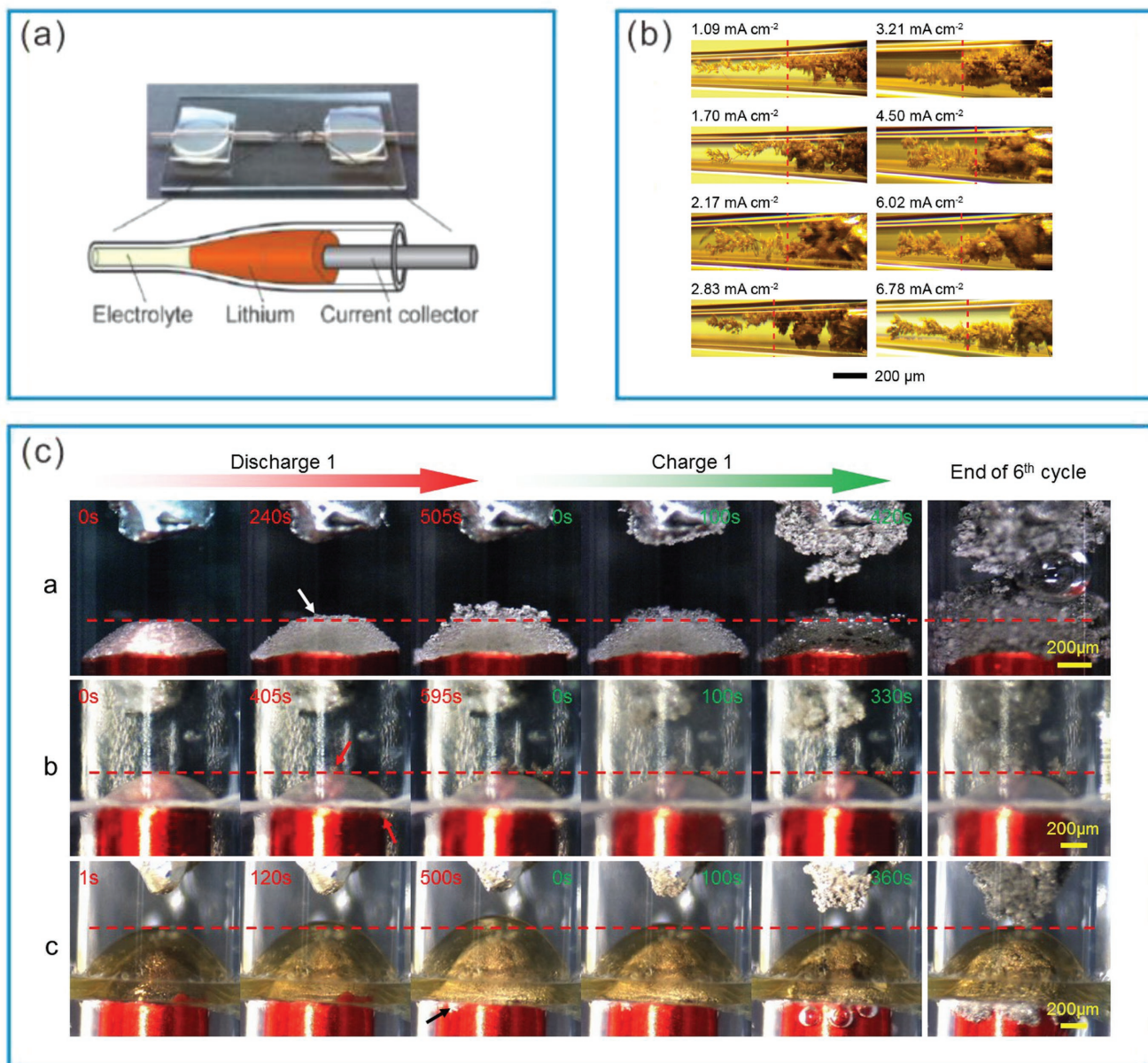


Figure 11. Examples of in situ optical microscope studies. a) Setup of capillary cell. b) “Representative optical images of lithium deposits demonstrating the clear change of morphologies at Sand’s time for various current densities.” Reproduced with permission.^[12] Copyright 2016, Royal Society of Chemistry. c) Real-time snapshots of capillary cells from the initial cycle to the end of the 6th cycle (from the first row to the third row: without any separator, with a polypropylene separator, with the rubber separator). Reproduced with permission.^[15] Copyright 2017, Royal Society of Chemistry.

how the electrochemical parameters affect LMI in its initiation and propagation.^[105] Kuo designed a transparent two-electrode cell, with a Raman spectroscopy detector to explore the surface condition of lithium metal anodes during cycling.^[106] The nucleation mechanism and morphology evolution of Li arms were investigated in different electrolytes and additives.

Although the optical microscopy and spectroscopy is an excellent tool to observe the morphologies of plating Li films, the spatial resolution of the in situ optical microscope is only micrometer-scale and above. With the advent of in situ electron microscopy, it is exciting for researchers to observe LMI more exquisitely from the nanoscale.

5.2. In Situ SEM Techniques

SEM has been the most widely used technique to analyze the surface modification of Li metal since 1970s because its resolution is as high as 1 nm and the size of battery for in operando tests is close to a normal battery. The SEM comprises of an electron source, a signal detector, lenses, a vacuum system and an observation platform that needs a visual battery structure and a thin film window (such as SiN_x membrane mm in diameter and tens of nm in thickness) transparent to electron beams, as illustrated in **Figure 12a**.^[107] Recently, by using even thinner window materials such as 2D materials, it was

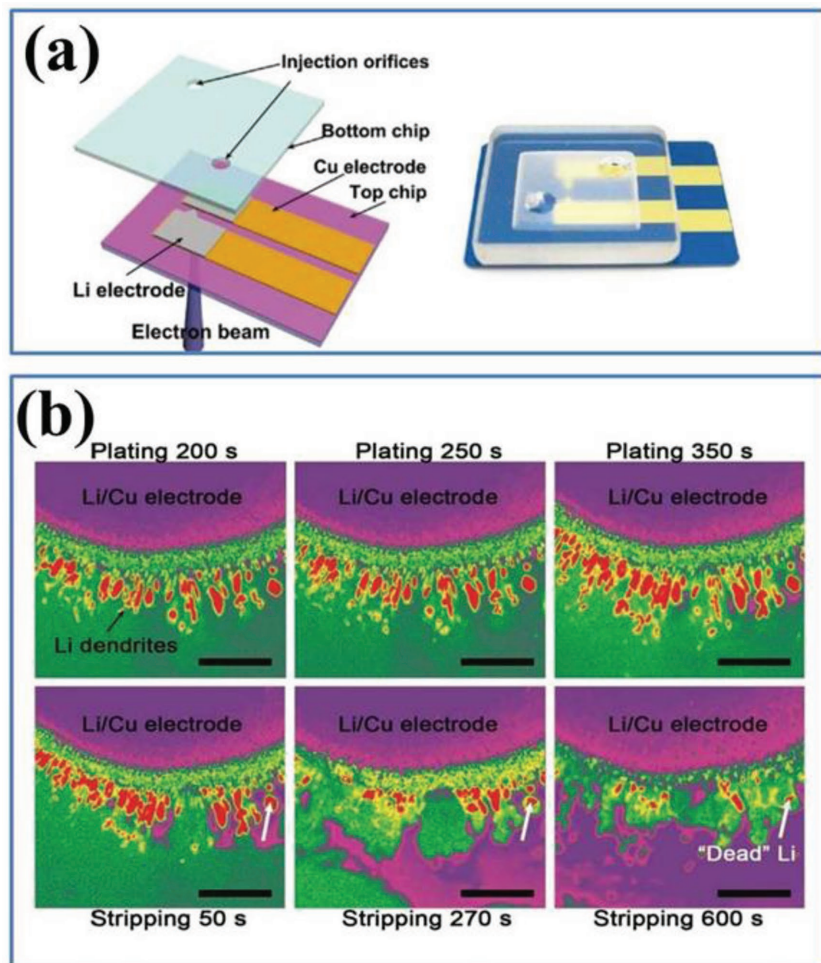


Figure 12. a) Bottom view (left) and top view (right) of a schematic in situ EC-SEM liquid cell. b) Representative snapshots of SEM images of the lithium plating/stripping processes: the three graphics in the first row demonstrate lithium plating and the three graphics in the second row represent “lithium stripping under 0.15 mA cm^{-2} on the Li/Cu electrode using the LiTFSI/DOL/DME electrolyte with the additive of LiNO_3 (1 wt%). The artificial colors of purple–green–yellow–red indicate the different contrasts from bright to dark in grayscale. The bright contrasts of Li/Cu electrode and the charged area are colored in red and yellow, respectively. Scale bar: $20 \mu\text{m}$.” Reproduced with permission.^[107] Copyright 2017, Wiley-VCH.

possible to perform in situ liquid SEM without a vacuum sample chamber (airSEM), with only 2% drop in contrast.^[108]

LMI through in situ SEM observations was first reported by Orsini et al.,^[109,110] who found the mossy and dendritic morphologies at the Li/electrolyte interface. Effects of additives,^[111] salts,^[112] solvents,^[113] and other treatments^[114,115] on LMI were then also investigated. It is found that the nucleation sites of Li metal was at solid/solid interfaces, and therefore the nuclei has to fight for space by pushing either electrode or electrolyte away.^[116] Recently, the lithium deposition/dissolution behaviors in liquid electrolytes was systematically studied by Rong through an “in situ electrochemical scanning electronic microscopy (EC-SEM)” (Figure 12b),^[107] who demonstrated that the additives in the electrolytes greatly affected the LMI growth rate and mechanisms. Specifically, a coaddition of both lithium nitrate and lithium polysulfide in the ether-based electrolyte remarkably minimized LMI growth.

5.3. In Situ Transmission Electron Microscopy (TEM) Techniques

Many processes in batteries are interface-limited, which makes direct observations of the SEI formation and Li plating at the electrode–electrolyte interface with high spatial resolution desirable for thorough understanding. In situ TEM equipped with selected area diffraction and electron energy-loss spectroscopy (EELS), allowing a direct visualization of lithiation combined with atomic spatial and on-line imaging,^[117] is an excellent choice for the dynamic observations of lithium stripping/plating at the nanoscale. Similar to in situ SEM characterizations, because the ordinary liquid electrolytes are easily evaporated in high-vacuum environment, it is necessary to seal the testing cells with a nanoscale membrane tens of nanometers thick so that electron beam can pass through,^[9,118,119] as designed by Kushima in the Figure 13a. In their experiments, the electron beam has to penetrate two silicon nitride membrane windows of about 100 nm combined thickness, as well as a liquid region of up to $1 \mu\text{m}$ thickness, before going through the TEM objective lens. This reduces the distinguishable morphological feature to $\approx 5 \text{ nm}$,^[120] a factor of ≈ 10 less than vacuum-based in situ TEM,^[121,122] but which is still far better than any other method for tracking spatial feature immersed in volatile liquid. The ability to perform EELS on samples immersed in liquid to identify valence state change further added to the power of this method.^[123]

Since 2010, when Huang et al. first demonstrated Li growth on various nanowire anodes,^[124] dendritic Li growth at nanoscale had been successively observed in real time by TEM.^[125] Later then, Yassar et al. reported a direct view of Li^+ nucleation at the lithium/electrolyte interface.^[126] However, the early in situ TEM investigations were mostly carried out using ionic liquid or solid-state electrolyte, whose SEI was quite distinct from those generated in the conventional liquid electrolytes. With the smartly designed microfluidic control, scientists start to perform real-time TEM investigations on Li dendrite growth in liquid battery cells.^[127–129] The direct proof of forming a SEI layer before Li deposition was discovered at the electrode–electrolyte interface.^[103,130] Using a homemade user-friendly in situ TEM holder, the “high-angle annular dark field STEM images of the anode/electrolyte interface during the first three charge–discharge cycles” were recorded, and some electrochemically dead Li residues that no longer adhering to the platinum electrode were found around the anode after Li stripping in every cycle.^[129]

Recently, Kushima et al. presented an in situ environmental transmission electron microscopy observation of metallic lithium deposition and dissolution in a liquid confining cell,^[9]

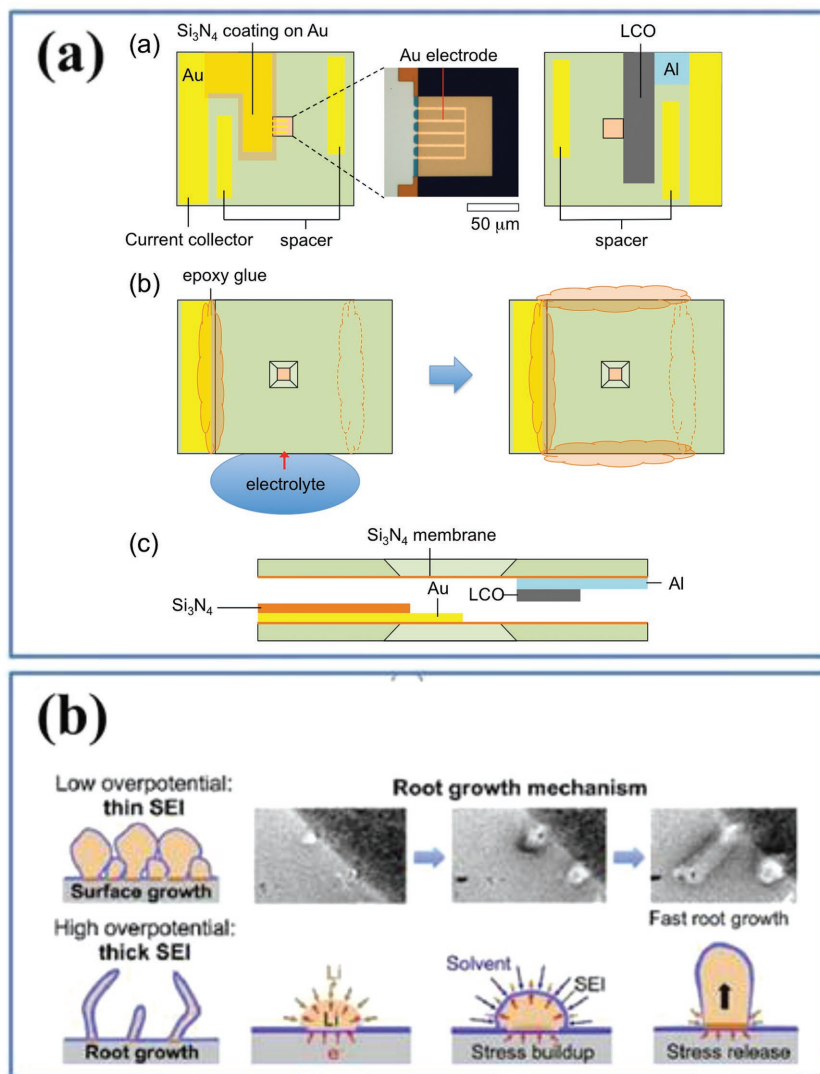


Figure 13. a) Configurations of the liquid confining cell, which are composed of two silicon chips: one of the silicon chips is lined with gold electrodes for observing the deposition of lithium, and the other silicon chip is a lithium cobalt electrode deposited on an aluminum foil to provide a lithium source for the battery. b) Root growth mechanism. Reproduced with permission.^[9] Copyright 2017, Elsevier B.V.

which indicated that the rate of SEI formation would obviously affect root versus surface growth mode. It is actually possible to visualize changes in the liquid electrolyte composition as it decomposes and the formation of the insoluble SEI passivation layer directly in real time, due to atomic number (Z) contrast.^[9] Root-growth versus tip-growth can be distinguished by tracking spatial features (such as attached or embedded nanoparticles) on the Li metal as fiducial makers. As illustrated in Figure 13b, upon delithiation, root-grown whiskers were highly unstable and the near-root Li metal segment usually dissolved first, generating a SEI stem at the root and rendering the rest of the whisker losing electrical contact. These electrically isolated dead lithium branches subsequently were easily swept away into the electrolyte to form “nano-lithium flotsam,” upon slight flow agitations. Those observations conformed to the proposed SEI-obstructed growth by two competing modes, namely dense

surface growth of cauliflowers (mode I) and root growth of lithium whiskers (mode II), as can be seen in Figure 1b.^[9]

5.4. Newly Developed in Situ Techniques

Transmission X-ray microscopy (TXM) is a powerful tool that operates under ambient conditions with a good spatial resolution. It has been utilized to investigate the morphology evolution of electrode materials for several years. An in situ observation of the lithium growth from nucleation and the subsequent development of lithium arms was reported by Cheng et al., who first visualized LMI on Cu surface through a versatile and facile experimental cell by operando TXM.^[131] Using a two-electrode transparent plastic cell, as shown in Figure 14a, it was found that at a current density of $\approx 1 \text{ mA cm}^{-2}$, evident growth and shrinkage of the mossy lithium were observed on the Cu surface, and meanwhile, the arms at base grew faster by increasing aspect ratio (height/width) during plating. In addition, the dendritic or mossy lithium is observed under the condition of various high current densities (25, 12.5, and 6.3 mA cm^{-2}) in different cycles, indicating nonuniform current distribution could induce a severe surface area proliferation (Figure 14b,c). “By coupling operando X-ray tomography and spatially resolved diffraction and absorption tomography” (Figure 15a), both chemical and morphological evolutions in the Li-S battery were investigated under realistic working conditions (Figure 15b).^[132] Indicated by Figure 15c, high heterogeneity of lithium deposition/dissolution was found in the lithium anode, and the profile changes of sulfur distribution were also tracked along the cathode depth.

While various dynamic characterization techniques have been developed on lithiation and deposition processes associated with the electrodes, less attention was paid to transport in the electrolyte under a wide range of temperature and current conditions, which played a significant role in the lithium deposition in the liquid electrolytes (Section 3.1). Recently, through in situ magnetic resonance imaging (MRI) (Figure 16a), Bazak et al. explored the influence of temperature on the steady-state electrolyte distribution at various current density with spatial resolution.^[133] Considering inhomogeneous initial concentration and “dead space” caused by the presence of conductive components such as the current collectors and electrodes, pure phase-encoding MRI techniques were utilized to circumvent this issue for the in situ cell designs.^[133] Finally, concentration profiles and its buildup rate were tracked (Figure 16b), which turned out to be noticeably temperature-dependent as shown in Figure 16c, consistent with predictions

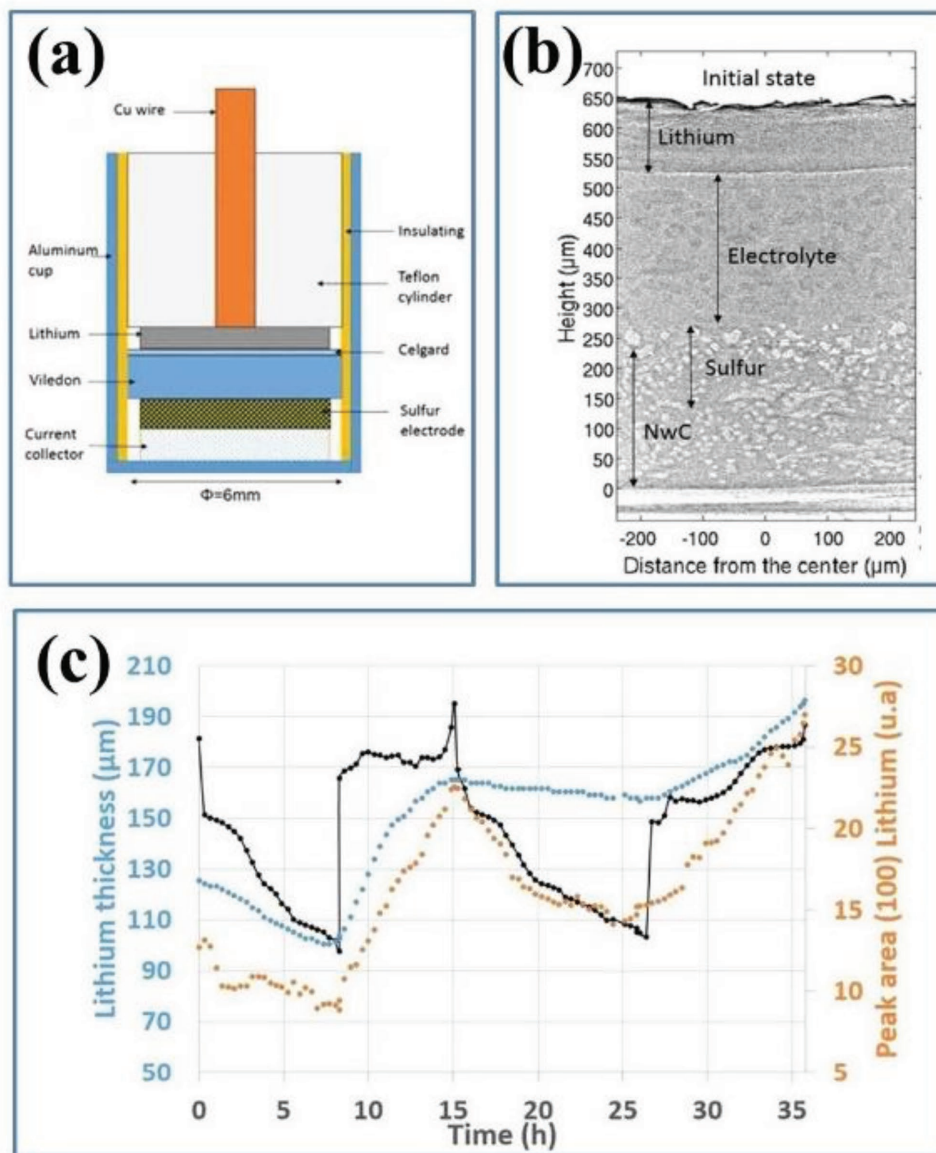


Figure 14. a) In operando TXM setups. b) In situ TXM images of lithium plating. The plating/stripping current density of the first, second, third row are 25, 12.5, and 6.3 mA cm^{-2} , respectively. The black and red arrows in the second row show the first-cycle dendritic lithium and the second-cycle mossy lithium, respectively. The blue arrow in the third row shows the third-cycle mossy lithium. All the images share the same scale bar as in the first row, which is $2.5 \mu\text{m}$. c) The cycling curve of voltage and current versus time. Reproduced with permission.^[131] Copyright 2017, American Chemical Society.

of ex situ NMR as well as electrochemical characterization techniques.

6. Summary and Outlook

Lithium metal anodes hold great promises for replacing graphite anodes and also promoting the so-called post-lithium ion batteries, such as Li-S, Li-O, and other Li metal batteries utilizing intercalation cathodes. However, at the current stage, industry-scale deployment of lithium anodes is impeded by safety concerns and poor cycling performance. Thus, effective regulation of Li plating/stripping and suppression of LMI is the most important mission on the way to industry-scale

applications of LMBs. To reach this goal, a comprehensive understanding of the SEI formation and LMI is critically needed. In this review, we first provide a fundamental understanding of SEI formation (Section 2.1) and balance-of-plant principles in constructing LMB (Section 2.2) where the terminology of Coulombic inefficiency and prelithiation (“ $0.5 \times$ excess,” “ $2 \times$ excess,” etc.) is introduced. The benefits of LiF and high DFC are explained for constructing parsimonious Li excess and parsimonious electrolyte, high-performance, full-cells. This followed by a qualitative overview in Section 3.1 of the long-range transport induction of LMI (Sand’s extinction as the ionic strength goes to zero) where we distinguish between tip-grown true dendrite (mode III) from root-grown whisker (mode II), as well as stress developments and inelastic creep/fracture in the

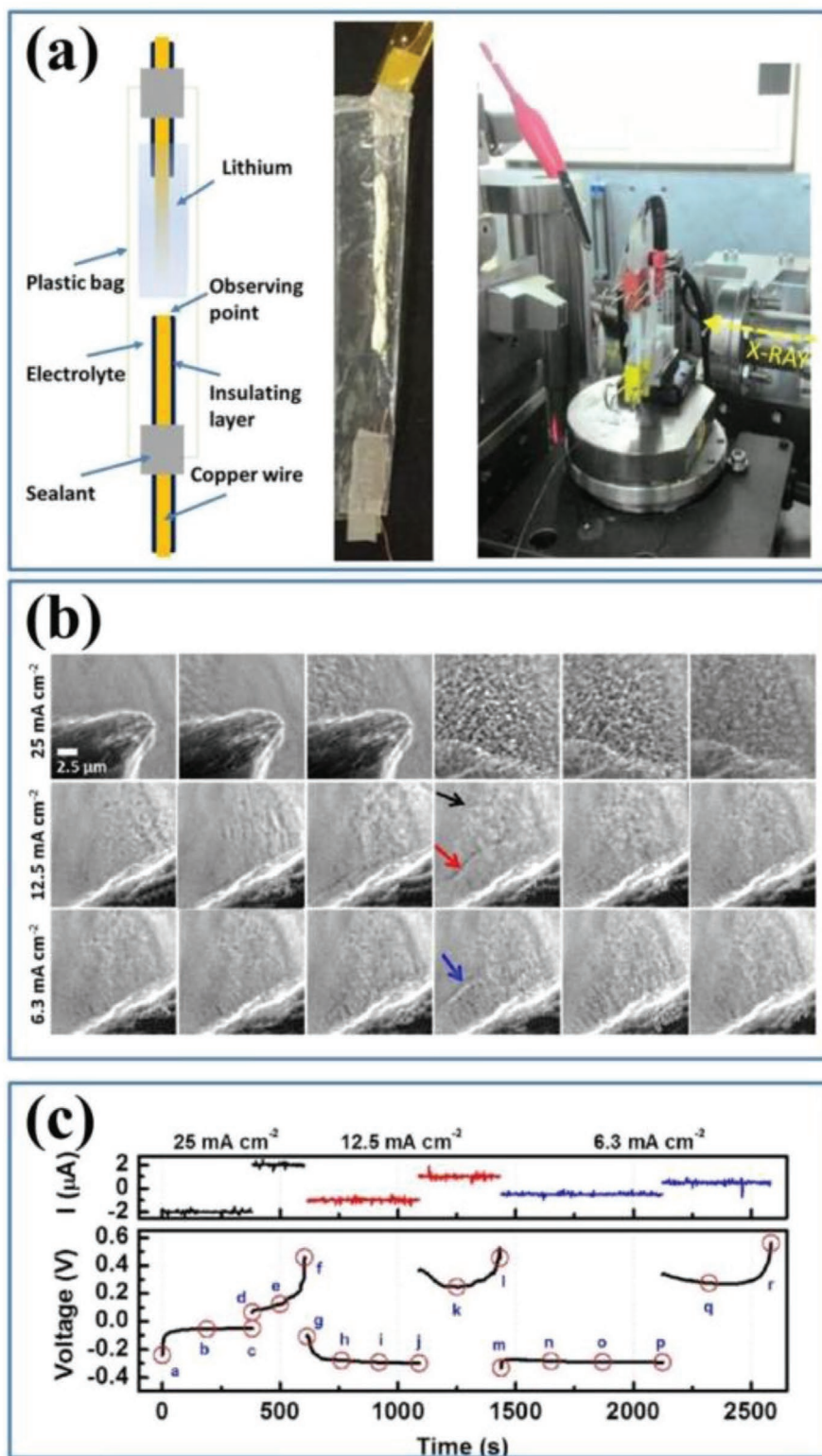


Figure 15. a) Schematic illustration of the operando cell. b) “Vertical slice of the tomographic cell at initial state with the associated X-ray diffraction (XRD) patterns. Light grey corresponds to high absorptive species (i.e., NwC and sulfur), whereas dark grey corresponds to less absorptive species (i.e., electrolyte and lithium).” Reproduced with permission.^[132] Copyright 2017, Nature Publishing Group. c) “Comparison between tomography and XRD lithium analysis with the associated voltage profile. Lithium thickness was calculated from the tomographic images by counting the number of pixels. Lithium peak area was integrated from XRD pattern at each time.” Reproduced with permission.^[132] Copyright 2017, Nature Publishing Group.

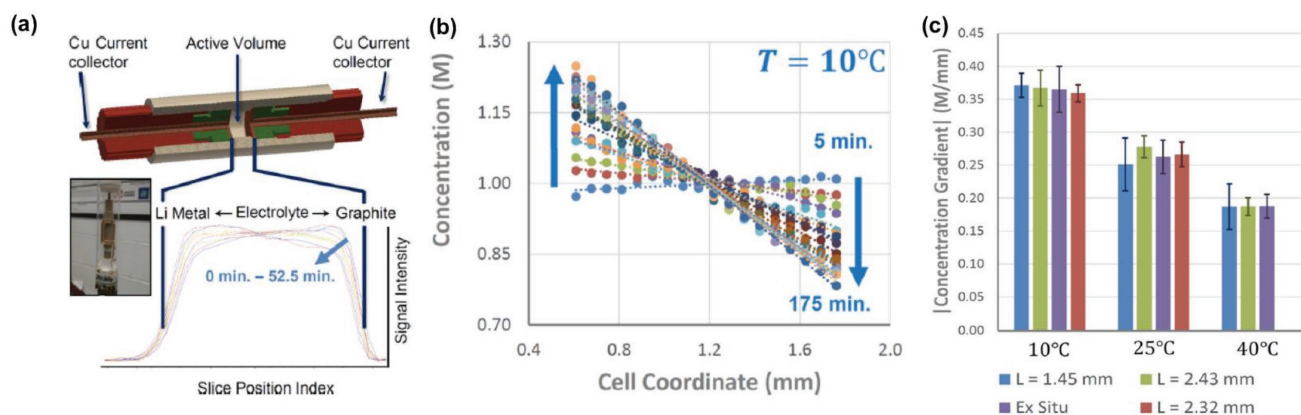


Figure 16. a) Schematic and photograph (inset) of the in situ MRI cell. b) Polarization buildup process of the in situ MRI cell at 10 °C (electrolyte: 1 M LiPF₆ in EC/PC/DMC; cell length: 2.43 mm; current density: 7.2 A m⁻²). c) “A comparison of the fitted CSI regression slopes for the concentration gradient magnitudes at three temperatures (10, 25, and 40 °C) and between the two nominal cell lengths (1.45 mm vs 2.43 mm and a 2.32 mm replicate)”. Reproduced with permission.^[133] Copyright 2017, American Chemical Society.

SEI and the Li metal, in Section 3.2. The take-home message is that low anion transference number t_- (delaying Sand’s singularity) and high ionic strength/salt concentration (reducing flammability and changing HOMO/LUMO levels) are desirable. Simultaneously, SEI fracture should be avoided by high-toughness nSEI, aSEI reinforcements, or 4S electrolyte, without increasing the cell impedance too greatly. Both discrete-agent-based and continuum numerical models of LMI were reviewed (Sections 3.3 and 3.4). A considerable number of experimental methods that were able to suppress LMI and enhance Coulombic efficiency have been shown (Section 4). Finally, recent progresses of the in situ characterization methods of the lithium deposition in LMBs, including in situ optical microscopy, electron microscopy observations as well as some other newly developed techniques, are highlighted (Section 5). In this review, particular attention is paid to the conceptual models (Sections 2, 3.1, and 3.2) as a reference to explore the effects of current density, electrolytes components, surface state of anodes on LMI, which also guide the lithium metal protection (Section 4) experimentally.

Although many breakthroughs have been attained, there are still many open challenges to be explored both theoretically and experimentally. From the SEI formation aspect, the as-formed nSEI film is usually a composite of organic and inorganics (Sections 4.1 and 4.2). The fundamental understanding of the nSEI formation mechanisms, its structure, chemical component, and regulation is still inadequate. The insights into the exact role of nSEI, the specific process of Li ions passing through SEI while stopping electron transport, and controllable modification of nSEI should be further improved. Moreover, in the long run, the SEI may be meticulously engineered to be an organic–inorganic composite like nacre in nature with superior toughness.^[134] This would be an ultimate example of a multifunctional material.

Until now, there has been no unified model for stress developments and inelastic deformations in Li metal and SEI (Section 3.2), or dead lithium arms and lithium flotsam accumulations (Section 3.4), to help to quantitatively predict the Coulombic inefficiencies of LMAs. Some models even contradict each other. Obviously, the Li-ion transport and mechanical

characteristics of the SEI (a nanoscale solid electrolyte layer), and the size-dependent plasticity of Li-metal grains and wires, need to be known before this is possible. It is absolutely critical in the future to develop more comprehensive numerical models to predict how LMI develops with multiple deposition–stripping cycles.

In next generation energy-dense lithium metal batteries, more than 4 mAh cm⁻² areal capacity of lithium metal anode is required (for lithium–sulfur batteries, the average working voltage of which is 50% lower, the areal capacity of lithium metal anode should be at least 5 mAh cm⁻²). However, the plating/stripping areal capacity of lithium metal in the current research literature is usually lower than 3 mAh cm⁻². Lower plating/stripping areal capacity usually brings apparently better protection effects if the cycle life is used as the sole criterion, which can be misleading. Meanwhile, although ultrasoft stretchy sticky solid electrolytes (Section 4.3) such as gels and 3D electrode frameworks (Section 4.4) suppress the lithium dendrites effectively, it inevitably lowers the volumetric energy density. Once the nonlithium fraction ϕ exceeds 70% (including the host structure), it will not be commercially competitive against graphite in terms of volumetric capacity, and therefore, when stabilizing lithium metal, the balance between gravimetric capacity and volumetric capacity should always be considered.

The lithium metal protection approaches are mostly based on coin cell, and how to extend them to large-scale Li metal foil or 3D host with prestored Li (prelithiated to “0.5 × excess,” “1 × excess,” “1.5 × excess,” etc., Section 2.2) should be considered. The emerging technologies for prelithiation in a roll-to-roll fashion should be considered. Also, how to optimize these individual strategies (high-DFC low-flammability liquid electrolyte, 4S gel electrolyte, aSEI, 3D electrode, etc.) and integrate them into a practical cell with good BOP is key. Graphite anode, with first-cycle Coulombic inefficiency of <10% and dropping quickly to <0.5% within 4 to 5 cycles, and with thickness increase of no more than 20% after thousands of cycles, is a formidable benchmark.

More and more resources are still being invested to rechargeable batteries. Competing anodes, such as Si, are also advancing along. In 1990s, lithium metal has already lost one

battle in industry-scale applications to graphite. Could this comeback be successful? More thorough understanding of Li plating/stripping behavior and practical strategies to suppress LMI are in high demand. We believe with continuous efforts devoted to the science and technology of lithium metal anodes, mass-market applications of LMBs may not be far away.

Acknowledgements

The authors are grateful for the guidance by Prof. Yunhui Huang, the support from Tongji University and the National Natural Science Foundation of China (NSFC Nos. 51602222 and 51632001). S.L. acknowledges the support by the Fundamental Research Funds for the Central Universities (No. 0500219233); J.L. acknowledges the support by NSF ECCS-1610806.

Conflict of Interest

The authors declare no conflict of interest.

Keywords

dendrite growth mode, donatable fluorine concentration, lithium metal protection, Sand's extinction, SEI fracture

Received: November 2, 2017

Revised: January 11, 2018

Published online: March 22, 2018

- [1] S. Chu, A. Majumdar, *Nature* **2012**, *488*, 294.
- [2] K. Amine, R. Kanno, Y. Tzeng, *MRS Bull.* **2014**, *39*, 395.
- [3] J. M. Tarascon, M. Armand, *Nature* **2001**, *414*, 359.
- [4] J. W. Choi, D. Aurbach, *Nat. Rev. Mater.* **2016**, *1*, 16013.
- [5] P. G. Bruce, S. A. Freunberger, L. J. Hardwick, J. M. Tarascon, *Nat. Mater.* **2011**, *11*, 19.
- [6] N. Nitta, F. Wu, J. T. Lee, G. Yushin, *Mater. Today* **2015**, *18*, 252.
- [7] H. J. S. Sand, *Philos. Mag.* **1901**, *1*, 45.
- [8] C. Brissot, M. Rosso, J. N. Chazalviel, S. Lascaud, *J. Power Sources* **1999**, *81–82*, 925.
- [9] A. Kushima, K. P. So, C. Su, P. Bai, N. Kuriyama, T. Maebashi, Y. Fujiwara, M. Z. Bazant, J. Li, *Nano Energy* **2017**, *32*, 271.
- [10] Y. Jin, S. Li, A. Kushima, X. Zheng, Y. Sun, J. Xie, J. Sun, W. Xue, G. Zhou, J. Wu, F. Shi, R. Zhang, Z. Zhu, K. So, Y. Cui, J. Li, *Energy Environ. Sci.* **2017**, *10*, 580.
- [11] S. Zhang, K. Zhao, T. Zhu, J. Li, *Prog. Mater. Sci.* **2017**, *89*, 479.
- [12] P. Bai, J. Li, F. R. Brushett, M. Z. Bazant, *Energy Environ. Sci.* **2016**, *9*, 3221.
- [13] J. B. Goodenough, Y. Kim, *Chem. Mater.* **2009**, *22*, 587.
- [14] E. Peled, D. Golodnitsky, G. Ardel, *J. Electrochem. Soc.* **1997**, *144*, L208.
- [15] K. Liu, P. Bai, M. Z. Bazant, C. A. Wang, J. Li, *J. Mater. Chem. A* **2017**, *5*, 4300.
- [16] G. Xu, Q.-b. Yan, S. Wang, A. Kushima, P. Bai, K. Liu, X. Zhang, Z. Tang, J. Li, *Chem. Sci.* **2017**, *8*, 6619.
- [17] W. W. Mullins, R. F. Sekerka, *J. Appl. Phys.* **1964**, *35*, 444.
- [18] A. N. Dey, *J. Electrochem. Soc.* **1970**, *117*, C248.
- [19] E. Peled, *J. Electrochem. Soc.* **1979**, *126*, 2047.
- [20] D. Aurbach, E. Zinigrad, Y. Cohen, H. Teller, *Solid State Ionics* **2002**, *148*, 405.
- [21] E. Peled, S. Menkin, *J. Electrochem. Soc.* **2017**, *164*, A1703.
- [22] X. B. Cheng, R. Zhang, C. Z. Zhao, Q. Zhang, *Chem. Rev.* **2017**, *117*, 10403.
- [23] M. D. Brennan, M. Breedon, A. S. Best, T. Morishita, M. J. S. Spencer, *Electrochim. Acta* **2017**, *243*, 320.
- [24] F. A. Soto, Y. Ma, J. M. Martinez de la Hoz, J. M. Seminario, P. B. Balbuena, *Chem. Mater.* **2015**, *27*, 7990.
- [25] X. B. Cheng, R. Zhang, C. Z. Zhao, F. Wei, J. G. Zhang, Q. Zhang, *Adv. Sci.* **2016**, *3*, 191.
- [26] S. Shi, P. Lu, Z. Liu, Y. Qi, L. G. Hector Jr., H. Li, S. J. Harris, *J. Am. Chem. Soc.* **2012**, *134*, 15476.
- [27] W. D. Richards, L. J. Miara, Y. Wang, J. C. Kim, G. Ceder, *Chem. Mater.* **2016**, *28*, 266.
- [28] L. Suo, W. Xue, M. Gobet, S. G. Greenbaum, C. Wang, Y. Chen, W. L. Yang, Y. X. Li, J. Li, *Proc. Natl. Acad. Sci. USA* **2018**, *115*, 1156.
- [29] G. Xu, A. Kushima, J. Yuan, H. Dou, W. Xue, X. Zhang, X. Yan, J. Li, *Energy Environ. Sci.* **2017**, *10*, 2544.
- [30] W. T. Gu, O. Borodin, B. Zdyrko, H. T. Lin, H. Kim, N. Nitta, J. X. Huang, A. Magasinski, Z. Milicev, G. Berdichevsky, G. Yushin, *Adv. Funct. Mater.* **2016**, *26*, 1507.
- [31] I. A. Shkrob, T. W. Marin, Y. Zhu, D. P. Abraham, *J. Phys. Chem. C* **2014**, *118*, 19661.
- [32] W. Xue, L. Miao, L. Qie, C. Wang, S. Li, J. Wang, J. Li, *Curr. Opin. Electrochem.* **2017**, *6*, 92.
- [33] M. D. Tikekar, S. Choudhury, Z. Tu, L. A. Archer, *Nat. Energy* **2016**, *1*, 16114.
- [34] Y. Zheng, Y. Wang, Y. Lu, Y.-S. Hu, J. Li, *Nano Energy* **2017**, *39*, 489.
- [35] Z. Zhu, A. Kushima, Z. Yin, L. Qi, K. Amine, J. Lu, J. Li, *Nat. Energy* **2016**, *1*, 16111.
- [36] C. Wang, X. Wang, Y. Yang, A. Kushima, J. Chen, Y. Huang, J. Li, *Nano Lett.* **2015**, *15*, 1796.
- [37] J. N. Chazalviel, *Phys. Rev. E* **1990**, *42*, 7355.
- [38] V. Fleury, J. N. Chazalviel, M. Rosso, *Phys. Rev. Lett.* **1992**, *68*, 2492.
- [39] V. Fleury, J. N. Chazalviel, M. Rosso, *Phys. Rev. E* **1993**, *48*, 1279.
- [40] C. Brissot, M. Rosso, J. N. Chazalviel, P. Baudryb, S. Lascaud, *Electrochim. Acta* **1998**, *43*, 1569.
- [41] X.-B. Cheng, C. Yan, J. Q. Huang, P. Li, L. Zhu, L. Zhao, Y. Zhang, W. Zhu, S. T. Yang, Q. Zhang, *Energy Storage Mater.* **2017**, *6*, 18.
- [42] L. Suo, Y. S. Hu, H. Li, M. Armand, L. Chen, *Nat. Commun.* **2013**, *4*, 1481.
- [43] C. Monroe, J. Newman, *J. Electrochem. Soc.* **2003**, *150*, A1377.
- [44] C. Monroe, J. Newman, *J. Electrochem. Soc.* **2004**, *151*, A880.
- [45] C. Monroe, J. Newman, *J. Electrochem. Soc.* **2005**, *152*, A396.
- [46] P. Barai, K. Higa, V. Srinivasan, *J. Electrochem. Soc.* **2016**, *164*, A180.
- [47] L. Tian, J. Li, J. Sun, E. Ma, Z.-W. Shan, *Sci. Rep.* **2013**, *3*, 2113.
- [48] J. Sun, L. He, Y. C. Lo, T. Xu, H. Bi, L. Sun, Z. Zhang, S. X. Mao, J. Li, *Nat. Mater.* **2014**, *13*, 1007.
- [49] T. Zhu, J. Li, *Prog. Mater. Sci.* **2010**, *55*, 710.
- [50] C. Xu, Z. Ahmad, A. Aryanfar, V. Viswanathan, J. R. Greer, *PNAS* **2017**, *114*, 57.
- [51] S. Kim, S. J. Choi, K. Zhao, H. Yang, G. Gobbi, S. Zhang, J. Li, *Nat. Commun.* **2016**, *7*, 10146.
- [52] M. Z. Meyers, J. W. Kaminski, T. F. Miller, *J. Phys. Chem. C* **2012**, *116*, 26214.
- [53] A. Aryanfar, D. Brooks, B. V. Merinov, W. A. Goddard, A. J. Colussi, M. R. Hoffmann, *J. Phys. Chem. Lett.* **2014**, *5*, 1721.
- [54] A. Aryanfar, D. J. Brooks, A. J. Colussi, B. V. Merinov, W. A. Goddard, M. R. Hoffmann, *Phys. Chem. Chem. Phys.* **2015**, *17*, 8000.
- [55] Q. Li, S. Tan, L. Li, Y. Lu, Y. He, *Sci. Adv.* **2017**, *3*, e1701246.
- [56] L. Liang, Y. Qi, F. Xue, S. Bhattacharya, S. J. Harris, L. Q. Chen, *Phys. Rev. E* **2012**, *86*, 051609.
- [57] L. Chen, H. W. Zhang, L. Y. Liang, Z. Liu, Y. Qi, P. Lu, J. Chen, L. Q. Chen, *J. Power Sources* **2015**, *300*, 376.

- [58] L. Liang, L. Q. Chen, *Appl. Phys. Lett.* **2014**, *105*, 263903.
- [59] D. R. Ely, R. E. Garcia, *J. Electrochem. Soc.* **2013**, *160*, A662.
- [60] D. R. Ely, A. Jana, R. E. García, *J. Power Sources* **2014**, *272*, 581.
- [61] A. Jana, R. E. García, *Nano Energy* **2017**, *41*, 552.
- [62] K. Xu, *Chem. Rev.* **2004**, *104*, 4303.
- [63] T. Placke, R. Kloepsch, S. Dühnen, M. Winter, *J. Solid. State Chem.* **2017**, *27*, 1939.
- [64] M. S. Park, S. B. Ma, D. J. Lee, D. Im, S. G. Doo, O. Yamamoto, *Sci. Rep.* **2014**, *4*, 3815.
- [65] D. Bedrov, O. Borodin, J. B. Hooper, *J. Phys. Chem. C* **2017**, *121*, 16098.
- [66] J. Wang, Y. Yamada, K. Sodeyama, C. H. Chiang, Y. Tateyama, A. Yamada, *Nat. Commun.* **2016**, *7*, 12032.
- [67] E. Markevich, G. Salitra, F. Chesneau, M. Schmidt, D. Aurbach, *ACS Energy Lett.* **2017**, *2*, 1321
- [68] J. Qian, W. A. Henderson, W. Xu, P. Bhattacharya, M. Engelhard, O. Borodin, J. G. Zhang, *Nat. Commun.* **2015**, *6*, 6362.
- [69] H. Kim, F. Wu, J. T. Lee, N. Nitta, H. T. Lin, M. Oschatz, W. I. Cho, S. Kaskel, O. Borodin, G. Yushin, *Adv. Energy Mater.* **2015**, *5*, 1401792.
- [70] L. E. Camacho-Forero, T. W. Smith, P. B. Balbuena, *J. Phys. Chem. C* **2017**, *121*, 182.
- [71] J. Zheng, J. A. Lochala, A. Kwok, Z. D. Deng, J. Xiao, *Adv. Sci.* **2017**, *4*, 1700032.
- [72] C. Wan, S. Xu, M. Y. Hu, R. Cao, J. Qian, Z. Qin, J. Liu, K. T. Mueller, J. G. Zhang, J. Z. Hu, *ACS Appl. Mater. Interfaces* **2017**, *9*, 14741.
- [73] C. B. Bucur, M. Jones, M. Kopylov, J. Spear, J. Muldoon, *Energy Environ. Sci.* **2017**, *10*, 905.
- [74] B. Wu, J. Lochala, T. Taverne, J. Xiao, *Nano Energy* **2017**, *40*, 34.
- [75] N. W. Li, Y. X. Yin, J. Y. Li, C. H. Zhang, Y. G. Guo, *Adv. Sci.* **2017**, *4*, 1600400.
- [76] H. Wang, M. Matsui, H. Kuwata, H. Sonoki, Y. Matsuda, X. Shang, Y. Takeda, O. Yamamoto, N. Imanishi, *Nat. Commun.* **2017**, *8*, 15106.
- [77] S. Zhang, M. J. Nava, D. G. Nocera, C. C. Cummins, unpublished.
- [78] X. Q. Zhang, X. B. Cheng, X. Chen, C. Yan, Q. Zhang, *Adv. Funct. Mater.* **2017**, *27*, 1605989.
- [79] H. Ye, Y. X. Yin, S. F. Zhang, Y. Shi, L. Liu, X. X. Zeng, R. Wen, Y. G. Guo, L. J. Wan, *Nano Energy* **2017**, *36*, 411.
- [80] F. Ding, W. Xu, G. L. Graff, J. Zhang, M. L. Sushko, X. Chen, Y. Shao, M. H. Engelhard, Z. Nie, J. Xiao, *J. Am. Chem. Soc.* **2013**, *135*, 4450.
- [81] X. B. Cheng, M. Q. Zhao, C. Chen, A. Pentecost, K. Maleski, T. Mathis, X. Q. Zhang, Q. Zhang, J. Jiang, Y. Gogotsi, *Nat. Commun.* **2017**, *8*, 336.
- [82] S. Choudhury, Z. Tu, S. Stalin, D. Vu, K. Fawole, D. Gunceler, R. Sundararaman, L. A. Archer, *Angew. Chem., Int. Ed.* **2017**, *56*, 13070.
- [83] X. Liang, Q. Pang, I. R. Kochetkov, M. S. Sempere, H. Huang, X. Sun, L. F. Nazar, *Nat. Energy* **2017**, *2*, 17119.
- [84] H. J. Peng, J. Q. Huang, X. B. Cheng, Q. Zhang, *Adv. Energy Mater.* **2017**, *7*, 1700260.
- [85] W. Li, H. Yao, K. Yan, G. Zheng, Z. Liang, Y.-M. Chiang, Y. Cui, *Nat. Commun.* **2015**, *6*, 7436.
- [86] X. B. Cheng, C. Yan, H. J. Peng, J. Q. Huang, S. T. Yang, Q. Zhang, *Energy Storage Mater.* **2017**, *10*, 199.
- [87] G. Zheng, S. W. Lee, Z. Liang, H. W. Lee, K. Yan, H. Yao, H. Wang, W. Li, S. Chu, Y. Cui, *Nat. Nanotechnol.* **2014**, *9*, 618.
- [88] L. Shi, A. Xu, T. Zhao, *ACS Appl. Mater. Interfaces* **2017**, *9*, 1987.
- [89] J. Lang, J. Song, L. Qi, Y. Luo, X. Luo, H. Wu, *ACS Appl. Mater. Interfaces* **2017**, *9*, 10360.
- [90] K. Liu, A. Pei, H. R. Lee, B. Kong, N. Liu, D. Lin, Y. Liu, C. Liu, P. C. Hsu, Z. Bao, Y. Cui, *J. Am. Chem. Soc.* **2017**, *139*, 4815.
- [91] C. Yang, B. Liu, F. Jiang, Y. Zhang, H. Xie, E. Hitz, L. Hu, *Nano Res.* **2017**, *10*, 4256.
- [92] Q. Li, S. Zhu, Y. Lu, *Adv. Funct. Mater.* **2017**, *27*, 1606422.
- [93] S. H. Wang, Y. X. Yin, T. T. Zuo, W. Dong, J. Y. Li, J. L. Shi, C. H. Zhang, N. W. Li, C. J. Li, Y. G. Guo, *Adv. Mater.* **2017**, *29*, 1703729.
- [94] L. L. Lu, J. Ge, J. N. Yang, S. M. Chen, H. B. Yao, F. Zhou, S. H. Yu, *Nano Lett.* **2016**, *16*, 4431.
- [95] Y. Li, J. Jiao, J. Bi, X. Wang, Z. Wang, L. Chen, *Nano Energy* **2017**, *32*, 241.
- [96] S. Jin, Z. Sun, Y. Guo, Z. Qi, C. Guo, X. Kong, Y. Zhu, H. Ji, *Adv. Mater.* **2017**, *29*, 1700783.
- [97] J. Lang, Y. Jin, X. Luo, Z. Liu, J. Song, Y. Long, L. Qi, M. Fang, Z. Li, H. Wu, *J. Mater. Chem. A* **2017**, *5*, 19168.
- [98] K. Yan, Z. Lu, H. W. Lee, F. Xiong, P. C. Hsu, Y. Li, J. Zhao, S. Chu, Y. Cui, *Nat. Energy* **2016**, *1*, 16010.
- [99] C. Yang, Y. Yao, S. He, H. Xie, E. Hitz, L. Hu, *Adv. Mater.* **2017**, *29*, 1702714.
- [100] C. Jin, O. Sheng, J. Luo, H. Yuan, C. Fang, W. Zhang, H. Huang, Y. Gan, Y. Xia, C. Liang, J. Zhang, X. Tao, *Nano Energy* **2017**, *37*, 177.
- [101] J. Zhao, G. Zhou, K. Yan, J. Xie, Y. Li, L. Liao, Y. Jin, K. Liu, P. C. Hsu, J. Wang, H. M. Cheng, Y. Cui, *Nat. Nanotechnol.* **2017**, *12*, 993.
- [102] S. S. Chi, Y. Liu, W. L. Song, L. Z. Fan, Q. Zhang, *Adv. Funct. Mater.* **2017**, *27*, 1700348.
- [103] Y. Yuan, K. Amine, J. Lu, R. Shahbazianyassar, *Nat. Commun.* **2017**, *8*, 15806.
- [104] T. Osaka, T. Homma, T. Momma, H. Yarimizu, *J. Electroanal. Chem.* **1997**, *421*, 153.
- [105] D. X. Liu, S. Frisco, P. Mandal, J. Whitacre, S. Litster, C. T. Love, K. Swider-Lyons, presented at *229th ECS Meeting*, San Diego, CA, USA, June **2016**.
- [106] L. M. Kuo, W. T. Lo, B. J. Hwang, J. H. Cheng, W. N. Su, A. A. Assegie, presented at *232nd ECS Meeting*, National Harbor, MD, USA, October **2017**.
- [107] G. Rong, X. Zhang, W. Zhao, Y. Qiu, M. Liu, F. Ye, Y. Xu, J. Chen, Y. Hou, W. Li, *Adv. Mater.* **2017**, *29*, 1606187.
- [108] Y. Han, K. X. Nguyen, Y. Ogawa, J. Park, D. A. Muller, *Nano Lett.* **2016**, *16*, 7427.
- [109] F. Orsini, A. D. Pasquier, B. Beaudoin, J. M. Tarascon, M. Trentin, N. Langenhuizen, E. D. Beer, P. Notten, *J. Power Sources* **1998**, *76*, 19.
- [110] F. Orsini, A. D. Pasquier, B. Beaudoin, J. M. Tarascon, M. Trentin, N. Langenhuizen, E. D. Beer, P. Notten, *J. Power Sources* **1999**, *81*, 918.
- [111] M. L. Yong, J. E. Seo, Y. G. Lee, H. L. Sang, K. Y. Cho, J. K. Park, *Electrochem. Solid-State Lett.* **2007**, *10*, A216.
- [112] Y. Li, C. Smith, C. Patrissi, C. R. Schumacher, B. L. Lucht, *J. Power Sources* **2008**, *185*, 1359.
- [113] G. Bieker, M. Winter, P. Bieker, *Phys. Chem. Chem. Phys.* **2015**, *17*, 8670.
- [114] J. K. Stark, Y. Ding, P. A. Kohl, *J. Electrochem. Soc.* **2011**, *158*, A1100.
- [115] R. S. Thompson, D. J. Schroeder, C. M. López, S. Neuhold, J. T. Vaughan, *Electrochem. Commun.* **2011**, *13*, 1369.
- [116] M. Motoyama, T. Kimura, Y. Iriyama, presented at *PRIME Meeting*, Honolulu, HI, USA, October **2016**.
- [117] H. W. Lee, Y. Li, Y. Cui, *Curr. Opin. Chem. Eng.* **2016**, *12*, 37.
- [118] J. N. De, F. M. Ross, *Nat. Nanotechnol.* **2011**, *6*, 695.
- [119] M. Sun, H. G. Liao, K. Niu, H. Zheng, *Sci. Rep.* **2013**, *3*, 3227.
- [120] A. Kushima, T. Koido, Y. Fujiwara, N. Kuriyama, N. Kusumi, J. Li, *Nano Lett.* **2015**, *15*, 8260.

- [121] J. Y. Huang, Y. C. Lo, J. J. Niu, A. Kushima, X. Qian, L. Zhong, S. X. Mao, J. Li, *Nat. Nanotechnol.* **2013**, *8*, 277.
- [122] X. H. Liu, Y. Liu, A. Kushima, S. Zhang, T. Zhu, J. Li, J. Y. Huang, *Adv. Energy Mater.* **2012**, *2*, 722.
- [123] M. E. Holtz, Y. Yu, D. Gunceler, J. Gao, R. Sundaraman, K. A. Schwarz, T. A. Arias, H. D. Abruña, D. A. Muller, *Nano Lett.* **2014**, *14*, 1453.
- [124] J. Y. Huang, L. Zhong, C. M. Wang, J. P. Sullivan, W. Xu, L. Q. Zhang, S. X. Mao, N. S. Hudak, X. H. Liu, A. Subramanian, H. Y. Fan, L. Qi, A. Kushima, J. Li, *Science* **2010**, *330*, 1515.
- [125] X. H. Liu, L. Zhong, L. Q. Zhang, A. Kushima, S. X. Mao, J. Li, Z. Z. Ye, J. P. Sullivan, J. Y. Huang, *Appl. Phys. Lett.* **2011**, *98*, 19.
- [126] H. Ghassemi, M. Au, N. Chen, P. A. Heiden, R. S. Yassar, *Appl. Phys. Lett.* **2011**, *99*, 19.
- [127] M. Gu, L. R. Parent, B. L. Mehdi, R. R. Unocic, M. T. McDowell, R. L. Sacci, W. Xu, J. G. Connell, P. Xu, P. Abellan, *Nano Lett.* **2013**, *13*, 6106.
- [128] B. L. Mehdi, M. Gu, L. R. Parent, W. Xu, E. N. Nasybulin, X. Chen, R. R. Unocic, P. Xu, D. A. Welch, P. Abellan, *Microsc. Microanal.* **2014**, *20*, 484.
- [129] B. L. Mehdi, J. Qian, E. Nasybulin, C. Park, D. A. Welch, R. Faller, H. Mehta, W. A. Henderson, W. Xu, C. M. Wang, *Nano Lett.* **2015**, *15*, 2168.
- [130] K. Yan, Z. Lu, H. W. Lee, F. Xiong, P. C. Hsu, Y. Li, J. Zhao, S. Chu, Y. Cui, *Nat. Energy* **2016**, *1*, 16010.
- [131] J. H. Cheng, A. A. Assegie, C. J. Huang, M. H. Lin, A. M. Tripathi, C. C. Wang, M. T. Tang, Y. F. Song, W. N. Su, B. J. Hwang, *J. Phys. Chem. C* **2017**, *121*, 7761.
- [132] G. Tonin, G. Vaughan, R. Bouchet, F. Alloin, M. D. Michiel, L. Boutafa, J. F. Colin, C. Barchasz, *Sci. Rep.* **2017**, *7*, 516.
- [133] J. D. Bazak, S. A. Krachkovskiy, G. R. Goward, *J. Phys. Chem. C* **2017**, *121*, 20704.
- [134] U. G. K. Wegst, H. Bai, E. Saiz, A. P. Tomsia, R. O. Ritchie, *Nat. Mater.* **2014**, *14*, 23.